

**ASSESSMENT OF CORROSION BEHAVIOUR OF MACHINED  
SUPER DUPLEX STAINLESS STEEL OBTAINED WITH THREE  
DIFFERENT PVD COATED TOOLS**

**ASSESSMENT OF CORROSION BEHAVIOUR OF MACHINED  
SUPER DUPLEX STAINLESS STEEL OBTAINED WITH THREE  
DIFFERENT PVD COATED TOOLS**

BY

EDINEI LOCKS JUNIOR, B.ENG.

A Thesis Submitted to the School of Graduate Studies in Partial Fulfilment of the  
Requirements for the Degree Master of Applied Sciences

McMaster University, Hamilton, Ontario, Canada

McMaster University © Copyright by Edinei Locks Junior, August 2019

MASTER OF APPLIED SCIENCE (2019)

McMaster University

(MECHANICAL ENGINEERING)

Hamilton, Ontario, Canada

TITLE: ASSESSMENT OF CORROSION BEHAVIOUR OF  
MACHINED SUPER DUPLEX STAINLESS STEEL  
OBTAINED WITH THREE DIFFERENT PVD COATED  
TOOLS

AUTHOR: Edinei Locks Junior, B. Eng., Mechanical Engineering

SUPERVISOR: Dr Stephen C. Veldhuis  
Department of Mechanical Engineering  
McMaster University

NUMBER OF PAGES: xiii, 104

## **ABSTRACT**

Super Duplex Stainless Steels (SDSS) are widely used in offshore oil and gas industrial components. They are dual phase materials consisting of ferrite and austenite in similar ratios with high contents of chromium and presence of molybdenum. This combination of microstructure and chemical composition results in enhanced mechanical strength and corrosion resistance. However, this material has poor machinability, exhibiting the following characteristics: (i) tendency to strain-harden; (ii) extreme adhesive behaviour; and (iii) high cutting temperatures. These circumstances not only result in high tool wear rates, but also lead to poor surface integrity due to the work hardening effect, high roughness and tensile residual stress. To minimize these detrimental effects, PVD coating technologies have been widely applied to cutting tools due to their tribological properties exhibited during cutting, which reduce friction and diminish heat. In this work, three different PVD coatings were tested during the turning of super duplex stainless steel of grade UNS S32750. In addition to the tool performance, surface integrity was assessed by surface texture analysis, residual stresses and hardness profile. The electrochemical behaviour of the machined surface was evaluated by potentiodynamic anodic polarization measurements. Stress cracking corrosion (SCC) tests were also performed. Results indicate a relationship between the tool performance and surface electrochemical behaviour, where the tool with best cutting performance, AlTiN, also presented the best electrochemical behaviour.

Stress cracking corrosion was found to be associated with residual stresses on the workpiece, among the three tested PVD coated tools the AlCrN/TiSiN showed lowest tensile residual stresses and lowest SCC susceptibility. The surface generated by AlTiN coated tool presented the highest levels of tensile residual stresses, resulting in a higher SCC susceptibility.

## **ACKNOWLEDGEMENT**

Firstly, I would like to express my sincere gratitude to Dr Stephen Veldhuis, not only for his supervision and support, but also for the unique and precious learning opportunity of the last two years and Dr Joseph Kish, for his distinguished guidance with corrosion experiments, which would not be possible without his assistance.

Secondly, a more than special thanks to: Dr Jose Mario Paiva for his guidance and friendship over the past years; Dr German Fox-Rabinovich, the owner of a brilliant mind that provided valuable support for this work; Dr Julia Dosbaeva for her assistance in many characterizations; the Machining Systems Laboratory staff, Mr. Terry Wagg, Steve Remilli, Brady Sample and Simon Oomen-Hurst for all their efforts to keep an excellent work environment in the lab, as well as personal and technical support.

I would also like to thank all the friends that I made in Canada, my lab mates and all people that not only made a contribution to this work, but also provided personal support. In particular, my roommate Pietro Stolf for the friendship and mutual support since the beginning of undergrad back home.

My special thanks to NSERC-CANRIMT for the financial support of my studies through the project number NETGP 479639-15.

Finally, but not less important, I'd like to thank to my family and friends back home. Their memory and endless care provided crucial emotional support.

## CONTENTS

|   |             |
|---|-------------|
| <b>ABSTRACT.....</b>                      | <b>iii</b>  |
| <b>ACKNOWLEDGEMENT.....</b>               | <b>v</b>    |
| <b>CONTENTS.....</b>                      | <b>vi</b>   |
| <b>LIST OF FIGURES.....</b>               | <b>ix</b>   |
| <b>LIST OF TABLES.....</b>                | <b>xiii</b> |
| <b>NOMECLATURE.....</b>                   | <b>xiv</b>  |
| <b>THESIS OUTLINE.....</b>                | <b>xvi</b>  |
| <b>CHAPTER 1 – INTRODUCTION.....</b>      | <b>1</b>    |
| 1.1 - MOTIVATION.....                     | 2           |
| 1.2 - RESEARCH OBJECTIVES.....            | 4           |
| <b>CHAPTER 2 – LITERATURE REVIEW.....</b> | <b>5</b>    |
| 2.1 – SUPER DUPLEX STAINLESS STEELS.....  | 5           |
| 2.1.1 – General characteristics.....      | 5           |
| 2.1.2 – SDSS microstructure.....          | 8           |
| 2.1.3 – Effects of alloying elements..... | 11          |
| 2.1.4 – Mechanical properties.....        | 13          |
| 2.1.5 – Physical properties.....          | 14          |

|   |           |
|---|-----------|
| 2.2 – MACHINING.....  | 14        |
| <b>2.2.1 – General aspects of metal cutting.....</b>          | <b>15</b> |
| <b>2.2.2 – Friction.....</b>                                  | <b>17</b> |
| <b>2.2.3 – Cutting temperatures.....</b>                      | <b>17</b> |
| <b>2.2.4 – Cutting forces.....</b>                            | <b>18</b> |
| <b>2.2.5 – Machinability of stainless steels.....</b>         | <b>20</b> |
| 2.3 – CUTTING TOOLS .....                                     | 21        |
| <b>2.3.1 – Tool wear .....</b>                                | <b>21</b> |
| <b>2.3.2 – Coating technologies.....</b>                      | <b>23</b> |
| 2.4 – SURFACE INTEGRITY AFTER MACHINING .....                 | 24        |
| <b>2.4.1 – Surface topography and texture .....</b>           | <b>25</b> |
| <b>2.4.2 – Residual stresses.....</b>                         | <b>26</b> |
| 2.5 – CORROSION .....   | 27        |
| <b>2.5.1 – Definitions.....</b>                               | <b>28</b> |
| <b>2.5.2 – Polarization and passivity .....</b>               | <b>29</b> |
| <b>2.5.3 – Corrosion of super duplex stainless steel.....</b> | <b>31</b> |
| 2.6 – STATE OF THE ART .....                                  | 34        |
| <b>CHAPTER 3 – METHODOLOGY .....</b>                          | <b>36</b> |
| 3.1 – WORKPIECE CHARACTERIZATION .....                        | 37        |

|  |           |
|--|-----------|
| 3.2 – CUTTING TESTS.....                                 | 39        |
| 3.3 – SURFACE INTEGRITY .....                            | 42        |
| <b>3.3.1 – Surface texture .....</b>                     | <b>42</b> |
| <b>3.3.2 – Hardness profile.....</b>                     | <b>43</b> |
| <b>3.3.3 – Residual stresses.....</b>                    | <b>43</b> |
| 3.4 – CORROSION TESTS.....                               | 44        |
| <b>3.4.1 – Potentiodynamic anodic polarizations.....</b> | <b>45</b> |
| <b>3.4.2 – Stress cracking corrosion .....</b>           | <b>47</b> |
| <b>CHAPTER 4 – RESULTS AND DISCUSSION.....</b>           | <b>49</b> |
| 4.1 – CUTTING TESTS.....                                 | 49        |
| 4.2 – SURFACE INTEGRITY .....                            | 56        |
| 4.3 – CORROSION TESTS.....                               | 67        |
| <b>CHAPTER 5 – CONCLUSIONS.....</b>                      | <b>82</b> |
| <b>CHAPTER 6 – SUGGESTION TO FUTURE WORKS .....</b>      | <b>84</b> |
| <b>REFERENCES .....</b>                                  | <b>85</b> |
| <b>APPENDIX .....</b>                                    | <b>93</b> |

## LIST OF FIGURES

|   |    |
|---|----|
| Figure 1: Super duplex stainless steel microstructure under SEM. Ferritic matrix with islands of austenite.....   | 6  |
| Figure 2: Schaeffler diagram [based on [16]].....   | 9  |
| Figure 3: Fe-Cr-Ni system phase diagram [based on [17]].  | 10 |
| Figure 4: Secondary phases chi, sigma and secondary austenite among ferrite grains [reprinted from [8], with permission].   | 11 |
| Figure 5: Primary, secondary and tertiary cutting zones schematics [based on [25]].   | 16 |
| Figure 6: Turning forces directions [based on [26]].....  | 19 |
| Figure 7: Tool wear types on cutting tools [reprinted from [19] with permission]: (a) flank wear; (b) crater wear; (c) notch wear; (d) nose radius; (e) thermal cracks; (f) mechanical cracks; (g) built-up edge; (h) plastic deformation; (i) edge chipping; (j) chip hammering; (k) gross fracture. | 23 |
| Figure 8: Arithmetic average roughness parameter Ra [based on [29]].  | 25 |
| Figure 9: Typical polarization curve [based on [30]].   | 31 |
| Figure 10: Typical pitting corrosion geometry [based on [30]].  | 32 |
| Figure 11: Intergranular (a) and transgranular (b) stress corrosion cracking propagation diagram [based on [30]].   | 33 |
| Figure 12: Experimental plan schematics.  | 37 |
| Figure 13: UNS S32750 microstructure.   | 39 |

|  |    |
|--|----|
| Figure 14: Workpiece shape and dimensions.....   | 40 |
| Figure 15: Cutting and feed direction of SDSS machined sample. ....  | 44 |
| Figure 16: Electrolytic cell setup (a) and sample (b) used in the polarization measurements.....   | 46 |
| Figure 17: Tool life results given by flank wear versus cutting length. ....   | 50 |
| Figure 18: Worn turning tools SEM analysis: (a) AlCrN/TiSiN, (b) AlCrN and (c) AlTiN.....  | 51 |
| Figure 19: AlTiN coated tool XPS analysis (a) point selected for the analysis on the tool's rake face (b) full XPS spectra and (c) high resolution Al2s peak XRD spectra. .... | 53 |
| Figure 20: Acquired cutting forces versus tool life stage. ....  | 54 |
| Figure 21: Surface texture produced with (a) AlCrN/TiSiN, (b) AlCrN, (c) AlTiN PVD coated tools and (d) mirror polished SDSS sample. ....                                      | 56 |
| Figure 22: Microhardness profile of AlCrN, AlCrN/TiSiN, AlTiN and SDSS samples. ....   | 58 |
| Figure 23: Residual stress measurements of AlCrN, AlCrN/TiSiN, AlTiN and SDSS samples. ....  | 60 |
| Figure 24: Compressive residual stress mechanism diagram. ....   | 61 |
| Figure 25: Tensile residual stress mechanism diagram.....  | 63 |
| Figure 26: Thermal barrier effect schematics. ....   | 64 |

|   |    |
|---|----|
| Figure 27: AlCrN/TiSiN coated tool XPS analysis (a) point selected for the analysis on the tool's rake face (b) full XPS spectra and (c) high resolution Si2s peak XRD spectra.....                       | 66 |
| Figure 28: Typical open circuit potential versus time for of AlCrN, AlCrN/TiSiN, AlTiN and SDSS samples.....  | 67 |
| Figure 29: Typical polarization curves of AlCrN, AlCrN/TiSiN, AlTiN and SDSS samples.....   | 68 |
| Figure 30: Corrosion potential (a) and current density (b) statistics.....  | 69 |
| Figure 31: Passivation potential (a) and current density (b) statistics.....  | 71 |
| Figure 32: Passive stage potential (a) and current density (b) statistics.....  | 73 |
| Figure 33: Transpassive potential (a) and current density (b) statistics.....   | 75 |
| Figure 34: Atomic Cr content on the machined samples surface.....   | 77 |
| Figure 35: Crack density after the SCC test.....  | 79 |
| Figure 36: Cracked surfaces.....  | 80 |
| Figure 37: Cracks cross-section optical analysis. AlCrN/TiSiN coated tool cutting (a) and (d) feed direction, AlCrN coated tool cutting (b) and (e) feed, AlTiN coated tool cutting (c) and (f) feed..... | 81 |
| Figure A1: OCP curve AlCrN sample 1.....  | 93 |
| Figure A2: OCP curve AlCrN sample 2.....  | 93 |
| Figure A3: OCP curve AlCrN sample 3.....  | 94 |
| Figure A4: OCP curve AlCrN/TiSiN sample 1.....  | 94 |
| Figure A5: OCP curve AlCrN/TiSiN sample 2.....  | 95 |

|  |     |
|--|-----|
| Figure A6: OCP curve AlCrN/TiSiN sample 3.....           | 95  |
| Figure A7: OCP curve AlTiN sample 1.....                 | 96  |
| Figure A8: OCP curve AlTiN sample 2.....                 | 96  |
| Figure A9: OCP curve AlTiN sample 3.....                 | 97  |
| Figure A10: OCP curve SDSS sample 1.....                 | 97  |
| Figure A11: OCP curve SDSS sample 2.....                 | 98  |
| Figure A12: OCP curve SDSS sample 3.....                 | 98  |
| Figure A13: Polarization curve AlCrN sample 1.....       | 99  |
| Figure A14: Polarization curve AlCrN sample 2.....       | 99  |
| Figure A15: Polarization curve AlCrN sample 3.....       | 100 |
| Figure A16: Polarization curve AlCrN/TiSiN sample 1..... | 100 |
| Figure A17: Polarization curve AlCrN/TiSiN sample 2..... | 101 |
| Figure A18: Polarization curve AlCrN/TiSiN sample 3..... | 101 |
| Figure A19: Polarization curve AlTiN sample 1.....       | 102 |
| Figure A20: Polarization curve AlTiN sample 2.....       | 102 |
| Figure A21: Polarization curve AlTiN sample 3.....       | 103 |
| Figure A22: Polarization curve SDSS sample 1.....        | 103 |
| Figure A23: Polarization curve SDSS sample 2.....        | 104 |
| Figure A24: Polarization curve SDSS sample 3.....        | 104 |

## LIST OF TABLES

|   |    |
|---|----|
| Table 1: Chemical requirements UNS S32750 [12]. .....                               | 7  |
| Table 2: Mechanical properties of UNS S32750 [17]. .....                            | 13 |
| Table 3: Thermal properties of different stainless-steel grades at 20 °C [17]. .... | 14 |
| Table 4: Chemical composition of UNS S32750 tubes (V&M Tubes). .....                | 37 |
| Table 5: PVD coatings composition and architecture. ....                            | 40 |

## **NOMECLATURE**

SDSS – Super duplex Stainless Steel

PVD – Physical Vapour Deposition

CVD – Chemical Vapour Deposition

PREN – Pitting Resistance Equivalent Number

ASTM – American Society for Testing and Materials

UNS – Unified Numbering System

SCC – Stress Corrosion Cracking

PSDZ – Primary Shear Deformation Zone

SSDZ – Secondary Shear Deformation Zone

TSDZ – Tertiary Shear Deformation Zone

$F_c$  – Cutting Force

$F_f$  – Feed Force

$F_z$  – Force in Z direction

SS – Stainless Steel

HSS – High Speed Steel

CBN – Cubic Boron Nitride

SI – Surface Integrity

$R_a$  – Average Surface Roughness

$E_{CORR}$  – Corrosion Potential

$E_P$  – Passivation Potential

CNC – Computer Numerical Control

$F_X$  – Force in X direction

$F_Y$  – Force in Y direction

DAQ – Data Acquisition

ISO – International Organization for Standardization

SEM – Scanning Electron Microscope/Microscopy

EDS – Energy Dispersive X-ray Spectroscopy

BUE – Built-up Edge

OCP – Open Circuit Potential

$i_{CORR}$  – Corrosion Current Density

$i_P$  – Passivation Current Density

$E_{PASS}$  – Passive potential

$i_{PASS}$  – Passive current density

$E_T$  – Transpassive potential

$I_T$  – Transpassive current density

## **THESIS OUTLINE**

This thesis is separated into six chapters, which are briefly described as follows:

**CHAPTER 1 – INTRODUCTION:** The motivation and the primary research objectives of this research are presented in this chapter.

**CHAPTER 2 – LITERATURE REVIEW:** All major concepts, theoretical references and other relevant studies are presented in this chapter to provide sufficient background for this research. This chapter can be separated into four main points: the material, the process, surface integrity and corrosion.

**CHAPTER 3 – EXPERIMENTAL PROCEDURE:** The methodology, experimental setups, test parameters and sampling are detailed in this chapter. The experimental procedure is separated into four parts: workpiece characterization, cutting tests, surface integrity evaluations and corrosion tests.

**CHAPTER 4 – RESULTS AND DISCUSSION:** The experimental results obtained in this study are presented and assessed in detail.

**CHAPTER 5 – CONCLUSIONS:** In this chapter, the main conclusions of the research will be stated on the basis of the results achieved during the experiments.

**CHAPTER 6 – SUGGESTION TO FUTURE WORKS:** Based on the results achieved in this study, other related aspects are recommended for future study.

## **CHAPTER 1 – INTRODUCTION**

The oil and gas industry represent a considerable share of the world economy and is still one of the primary sources of energy. Unique materials are used in the equipment and machinery throughout the entire chain of production, which feature enhanced mechanical properties and elevated corrosion resistance to handle the aggressive work conditions. Usually, offshore oil reserves are located up to 350 km from the coast and reach depths of up to 7 km, under a thick layer of marine water, rocks and salt. Components employed in the extraction process operate under an extremely corrosive environment, high mechanical loads (sea currents, internal and external pressures) and direct contact with a hard substrate. Preventing component failures in such applications requires strict material selection. New grades of stainless steels emerge as an ideal class of materials to be used in the components and pipelines for offshore oil extraction.

Considering the above requirements, super duplex stainless steel (SDSS) features enhanced mechanical properties and elevated corrosion resistance, which is ideal for the aforementioned applications. These outstanding material properties are associated with the presence of a dual microstructure composed of ferrite and austenite, as well as the high content of Cr as well as presence of Ni, Mo and N.

The manufacturing process of such components requires multiple machining operations. This is because during the cutting process, conventional

machining technologies are inadequate for SDSS workpiece materials, due to their high strain hardening tendency and low thermal conductivity. The cutting process of this material is strongly characterized by the high amount of material adhesion onto the rake face, elevated cutting forces and cutting temperature, as well as problematic chip formation/evacuation. The aforementioned issues could naturally promote severe damage in the machined surface due to excessive residual stresses and surface defects.

## 1.1 - MOTIVATION

Enterprises are continuously searching for solutions to improve the machining process of this material. A natural approach is the surface engineering of cutting tools via the deposition of a micrometric-thick layer of a composite material with enhanced mechanical and thermal properties, generally by means of Physical Vapour Deposition (PVD) or Chemical Vapour Deposition (CVD). These technologies provide extra wear protection to the tool substrate, increasing the tool life and productivity of the machining process [1].

However, tool life improvement is not the only concern of offshore oil extraction industry. Process performance is pointless if the manufacturing methods produce surface and material flaws that compromise the component functionality in terms of mechanical properties and corrosion resistance. Even if the material possesses elevated corrosion resistance, the combination of poor surface integrity,

external forces and corrosive atmosphere can lead to early component failure [2], [3]. A better understanding of surface integrity is needed to mitigate the poor performance and excessive maintenance of oil and gas systems.

The most important concern of the machined products used in oil and gas offshore operations is the control and prediction of corrosion behavior [4]. The main goal of this is to reduce excessive maintenance costs and lower the risk of complete oil extraction system failure that can cause an environmental catastrophe.

Tool wear performance, surface integrity after machining and material corrosion behaviour need to be evaluated and discussed in greater detail. This work seeks to understand the corrosion of SDSS components due to detrimental surface integrity states by selecting the appropriate coated cutting tools during the manufacturing process.

## 1.2 - RESEARCH OBJECTIVES

The main goal of this study is to evaluate the impact of the three PVD coated tools on the surface integrity and the localized corrosion susceptibility, including stress cracking corrosion (SCC) of SDSS. The specific research objectives in this work are described as it follows:

1. Tool life and wear analysis of an AlTiN and AlCrN monolayer PVD coated tool with an established benchmark AlCrN/TiSiN multilayer PVD coating during the turning process of super duplex stainless steel under finish cutting conditions.
2. Evaluation of the surface integrity in terms of surface roughness, work hardening and residual stresses of each machined surface produced by the coated tools.
3. Investigation of the localized corrosion susceptibility of machined super duplex stainless steel exposed to detrimental conditions.
4. Assessment of the effect of surface residual stress on the material's stress cracking corrosion susceptibility.

## **CHAPTER 2 – LITERATURE REVIEW**

### **2.1 – SUPER DUPLEX STAINLESS STEELS**

#### **2.1.1 – General characteristics**

Super duplex stainless steels are a grade of stainless steels whose microstructure is composed of ferrite ( $\alpha$ ) and austenite ( $\gamma$ ) in approximately equal volume fractions [5], [6] as shown in figure 1. This type of material has outstanding mechanical strength and excellent corrosion resistance due to its balanced microstructure and chemical composition rich in Cr, Ni, Mo and N [7]. The lower content of Ni when compared to another austenitic grades and presence of Mo and N, results in an alloy with lower cost and greater corrosion resistance. The combination of its two phases results in better corrosion resistance compared to purely ferritic stainless steel grades, as well as higher strength compared to purely austenitic ones [6], [8].

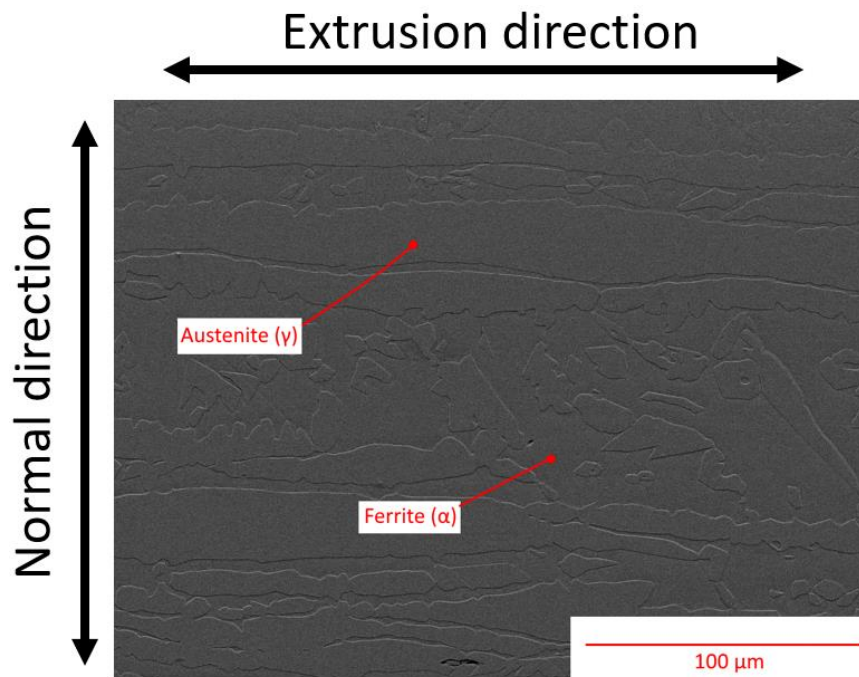


Figure 1: Super duplex stainless steel microstructure under SEM. Ferritic matrix with islands of austenite.

The corrosion resistance of SDSS can be attributed to the high content of alloying elements in its chemical composition. Despite their excellent pitting corrosion resistance, super duplex stainless steels are not invulnerable to corrosion, as microstructural defects, secondary phases and grain size play a relevant role [7].

The alloying elements that contribute the most to the localized corrosion susceptibility of SDSS are Cr, Mo and N. Differences in corrosion resistance can exist between ferrite and austenite which is given by two main factors: (i) selective distribution of the aforementioned elements in these phases [7], [9]; and (ii) the galvanic corrosion effect that the two phases can have among themselves [10].

The corrosion resistance of the material can be empirically evaluated via the Pitting Resistance Equivalent Number (PREN). This value is derived from equation 1, where the weight percentage of Cr, Mo and N are used as input [11]. It is important to note that Mo and N have a higher contribution for corrosion resistance than Cr, given by the multiplier factors.

$$PREN = \%Cr + 3.3\%Mo + 16\%N \quad \text{Equation 1}$$

Duplex stainless steel grades are expected to yield PREN values greater than 20, and super duplex stainless steels over 40 [12]. The typical chemical composition, according to ASTM A890/890M, of UNS S32750 stainless steel gives PREN values of around 42. The chemical requirements of this alloy are shown in Table 1 [12].

Table 1: Chemical requirements UNS S32750 [12].

| Chemical Requirements |                 |      |      |      |      |           |         |         |           |     |     |       |
|-----------------------|-----------------|------|------|------|------|-----------|---------|---------|-----------|-----|-----|-------|
| Material              | Elements (wt.%) |      |      |      |      |           |         |         |           |     |     |       |
| UNS S32750            | C               | Mn   | P    | S    | Si   | Cr        | Ni      | Mo      | N         | Co  | W   | Other |
|                       | 0.03            | 1.50 | 0.04 | 0.04 | 1.00 | 24.0-26.0 | 6.0-8.0 | 4.0-5.0 | 0.10-0.30 | N/A | N/A | N/A   |

Apart from its excellent corrosion resistance, this material is susceptible to localised pitting corrosion and even SCC [5], [13]. A well-balanced microstructure tends to reduce the susceptibility of both effects [14], [15]. The localized corrosion

and SCC susceptibility of SDSS is a subject of detailed analysis further in this study.

### **2.1.2 – SDSS microstructure**

The microstructure of super duplex stainless steel consists of an optimized combination of alloying elements as well as a controlled cooling process, which results in the stable formation of ferrite and austenite [5], [8]. A very convenient representation of the alloying elements in the microstructure of stainless steels is given by the Schaeffler diagram, which plots the boundaries of austenite, ferrite and martensite in terms of equivalent Cr and Ni at room temperature [16]. The equivalence of Cr and Ni is an empirical relation accounting for other elements that have the same function of Cr and Ni in the stainless steel microstructure [16].

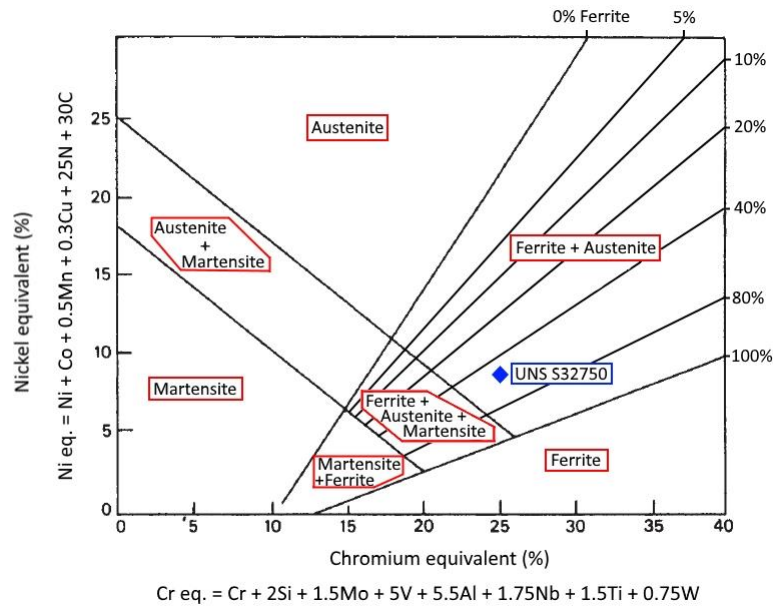


Figure 2: Schaeffler diagram [based on [16]].

The unbalanced alloying and processing of SDSS can cause the nucleation of undesired secondary phases in the material microstructure due to its complex precipitation behaviour [8]. According to Nilsson in super duplex stainless steel with 25%Cr and 7%Ni, the only phases that are thermodynamically stable between 1000°C and 1200°C are ferrite and austenite. A large variety of undesirable secondary phases are formed between 300°C and 1000°C. To illustrate the effect of temperature and composition, Figure 3 shows the phase diagram of the Fe-Cr-Ni system, where a microstructure of ferrite and austenite in the nucleating region is highlighted in green.

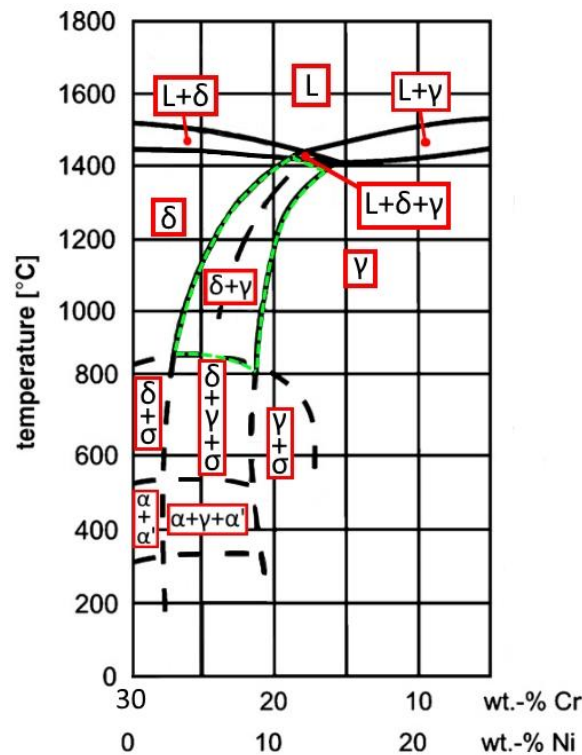


Figure 3: Fe-Cr-Ni system phase diagram [based on [17]].

Since ferrite has a higher diffusion rate, all relevant secondary phases precipitations can be found in this phase. A few different types of secondary phases can be found in the SDSS microstructure, with the most common being: sigma ( $\sigma$ ), chi ( $\chi$ ), alpha prime ( $\alpha'$ ), secondary austenitic ( $\gamma_2$ ), R phase and chromium nitrides. Their formation is the result of the diffusion of alloying elements out of ferrite and austenite, where each secondary phase has its mechanism and temperature range of formation. Their presence results in localised corrosion and ductility loss, tending towards to a brittle failure. Figure 4 shows some of the secondary phases in the SDSS matrix.

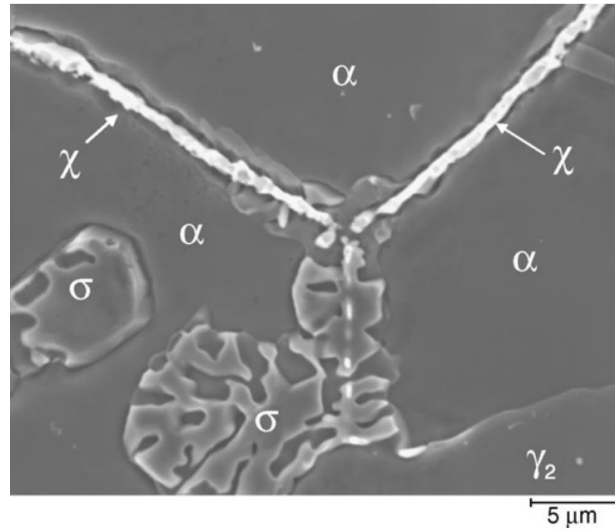


Figure 4: Secondary phases chi, sigma and secondary austenite among ferrite grains [reprinted from [8], with permission].

### 2.1.3 – Effects of alloying elements

Similar to other steels, stainless steels are iron-based alloys that have Cr and Ni as major alloying elements, making them resistant to oxidation in normal atmospheres [18]. Other alloying elements such as Mo, N, Ti, Si can be included to obtain specific properties. Some common alloying elements and their intended functions are briefly described below [18]–[20]:

- Chromium: Enhances corrosion resistance by forming a passive layer on the surface and improves the mechanical properties due to the hardening effect of the solid solution.

- Molybdenum: Stabilizes the ferrite formation. Increases pitting and crevice corrosion protection by the formation of molybdate ion film, improving the corrosion resistance in aggressive environments (acid/chlorides rich).
- Nickel: Accelerates the solid solution solidification process, resulting in higher ductility and extends the austenite stability range.
- Nitrogen: Increases the austenite corrosion resistance in acid environments and assists its formation when its composition is between 0.1-0.35%. It also delays the precipitation of intermetallic phases.
- Carbon: Elevates the material hardness and wear resistance by forming carbides with Ti, Ta and Ni also present in the chemical composition. Their content must be limited to prevent nucleation of detrimental chromium carbides.
- Sulfur: Though usually considered to be a contaminant, however in small amounts and associated with manganese, it forms manganese sulfide (MnS) which can improve machinability.
- Silicon addition between 0.5-5.0% improves wear and heat resistance. Tungsten usually increases the pitting corrosion resistance and helps avoid sigma phase nucleation.

### 2.1.4 – Mechanical properties

The mechanical properties of SDSS are a combination of the mechanical properties of ferrite and austenite [21]. The tensile strength of the alloy is more influenced by the ferrite due to its high values of yield strength. However, the nitrogen content in the austenite may contribute to the formation of a stronger phase than ferrite [22]. Additional strengthening is given by a hardening effect of the alloying elements [5]. Some tensile strengths along with elongation data, are displayed in Table 2.

The toughness of SDSS can be attributed to the ductile austenitic phase, which can impede ferrite fracture [5]. In terms of temperature, SDSS undergoes a transition from a ductile to brittle state near  $-50\text{ }^{\circ}\text{C}$ , becoming brittle above  $300\text{ }^{\circ}\text{C}$  due to the precipitation of secondary phases [9], [14], [23].

Table 2: Mechanical properties of UNS S32750 [17].

| Alloy        | UNS    | Stress at 0.2% elongation (MPa) | Ultimate Tensile Strength (MPa) | Elongation (min.) % |
|--------------|--------|---------------------------------|---------------------------------|---------------------|
| Austenitic   | S31603 | 170                             | 485                             | 40                  |
|              | S31254 | 300                             | 650                             | 35                  |
| Ferritic     | S40900 | 205                             | 380                             | 20                  |
|              | S44700 | 415                             | 550                             | 20                  |
| Super duplex | S32304 | 400                             | 600                             | 25                  |
|              | S32750 | 550                             | 795                             | 15                  |

### 2.1.5 – Physical properties

Similar to mechanical properties, the physical properties of SDSS lie in between those of ferritic and austenitic steels. They have higher thermal conductivity than austenitic stainless steels due to the presence of the ferritic phase. However, this results in less thermal expansion [17]. These characteristics are beneficial for thermal cyclic applications, where the working temperatures are under 300 °C. Table 3 shows the specific heat capacity and the thermal conductivity for an austenitic, a ferritic and a super duplex stainless steel grade.

Table 3: Thermal properties of different stainless-steel grades at 20 °C [17].

| Alloy        | UNS    | Specific heat capacity (J/Kg K) | Thermal conductivity (W/m K) | Thermal expansion coefficient ( $10^{-6}$ /K) |
|--------------|--------|---------------------------------|------------------------------|---|
| Austenitic   | S30400 | 520                             | 16                           | 16  |
| Ferritic     | S43000 | 480                             | 22                           | 10  |
| Super duplex | S32750 | 470                             | 14                           | 13  |

## 2.2 – MACHINING

As described by Trent et al. [24], the term metal cutting, or machining, describes operations where a thin layer of metal, the chip, is removed by a harder wedge-shaped tool from a larger body. This process is widely used in industry to shape metals and other materials for a wide range of applications at a cost of billions of dollars per year.

The cutting process is characterized by the relative movement between the tool along the workpiece promoting shearing and being governed by process parameters such as cutting speed, feed rate, tool engagement (depth of cut), tool geometry, cooling technique and workpiece material. Variations in these parameters will result in process output changes such as surface integrity, cutting temperatures and forces. In this section, the most essential metal cutting aspects will be discussed to understand the wear mechanisms and surface integrity during this process.

### **2.2.1 – General aspects of metal cutting**

The metal cutting process constitutes a complex behaviour, in which high strain rates, temperatures and forces are produced in the cutting zone. Regardless of their differences, all cutting processes have the same phenomena occurring in the cutting region. A schematic drawing of the cutting region is presented in Figure 5.

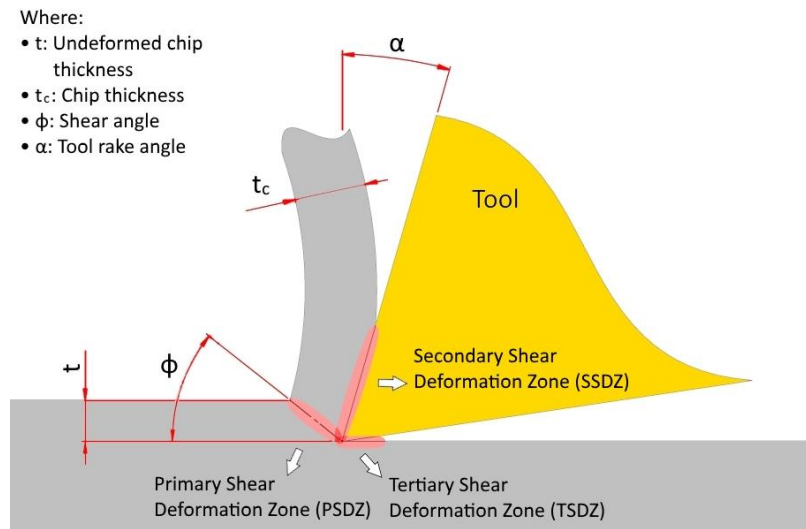


Figure 5: Primary, secondary and tertiary cutting zones schematics [based on [25]].

The diagram displayed in Figure 5 illustrates the main points of interest in the cutting zone, which are the three shear zones. In these areas, essential phenomena that govern the process take place. All plastic deformation associated with the metal cutting process occurs in the Primary Shear Deformation Zone (PSDZ), where a certain amount of material with volume  $V$  and thickness  $t$  is fed toward the cutting edge, suffering severe plastic deformation on the shear plane oriented at  $\phi$  degrees and consequently consuming a high amount of energy [26].

In the Secondary Shear Deformation Zone (SSDZ), frictional work takes place on the tool rake surface, where a portion of plastically deformed material (chip) with thickness  $t_c$  (where  $t_c$  is higher than  $t$ ) flows along the rake face (oriented by  $\alpha$  angle), generating extremely high stresses. The Tertiary Shear Deformation Zone (TSDZ) is created by the friction of the clearance face of the cutting tool with

the workpiece, which results on tool wear and directly affects the surface integrity of the machined surface [26].

### **2.2.2 – Friction**

The chip characteristics can carry useful information regarding the cutting process, where a considerable amount of friction energy is dissipated in the chip-tool region due to strong interaction with the tool. However, it is impossible to assess the phenomena that occur on the chip-tool interface by direct observation because this region of interest is obstructed by the material during the cut.

The flow of the chip over the tool promotes severe tribological conditions, directly influencing the chip-tool contact length, frictional and normal forces, shearing velocity and stress, as well as temperature and tool wear.

### **2.2.3 – Cutting temperatures**

Almost all the total energy produced by the cutting process is transformed into heat within the shear zones by plastic deformation and friction. Literature states that these effects are directly influenced by cutting parameters and workpiece materials. Additionally, the heat of each shear zone will affect the cutting process in a different way [25], [26].

The heat generated on the PSDZ has almost no influence on the tool temperature since a significant part of it is dissipated through chips and transferred into the workpiece. In excess amounts, it can lead to residual tensile stresses, contributing to crack initiation and propagation [26]. In case of SSDZ, the heat goes into the cutting tool, which accelerates the tool wear.

Therefore, to produce a part with adequate surface finish and acceptable tool life, it is necessary to have proper heat control. One method of providing heat resistance to the tool is surface engineering by means of coating deposition on the tool surface.

#### **2.2.4 – Cutting forces**

Cutting forces are an essential parameter of the machining process. Apart from determining the amount of power consumed during the cutting process, the cutting forces are the response of the combined effect of the system (clamping, materials, cutting conditions and cooling/lubrication). Cutting forces can be measured during machining as indicators of tool condition and material's machinability index [24], [26]. According to Trent et al. [24], the cutting forces are influenced by shear yield strength, other material properties and modifiers. In Figure 6, a tridimensional simple turning process is shown. Three force components are acting on the tool during this operation [24]:

- Cutting Force ( $F_c$ ): Acting in the cutting direction, perpendicular to the cutting edge.
- Feed Force ( $F_f$ ): Acting parallel to the feed direction.
- Force in Z direction ( $F_z$ ): Force component normal to the  $F_c$ - $F_f$  plane. It is the smallest component of the system and tends to push the tool away from the workpiece.

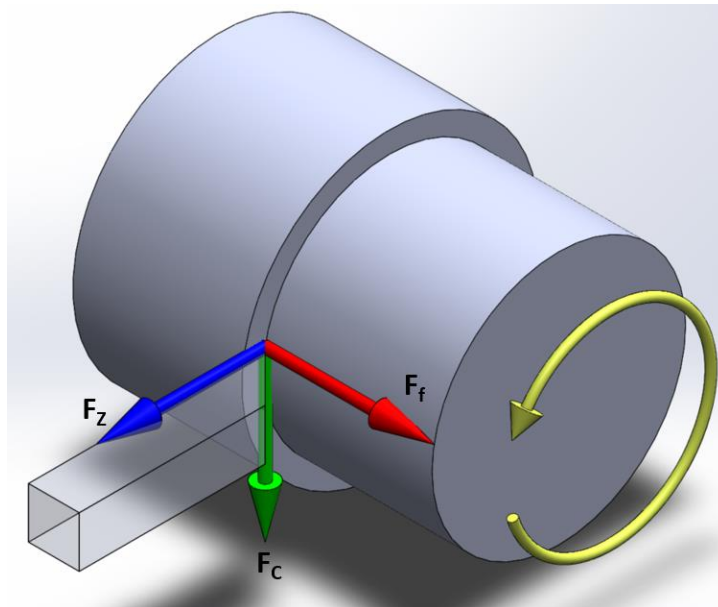


Figure 6: Turning forces directions [based on [26]].

The current technology used to assess the forces are quartz crystal dynamometers, specially designed for machine-tools. This technology replaced previous instruments, such as hydraulic and strain gauges, due to its better thermal stability and small cross-sensitivity between directions [26].

### **2.2.5 – Machinability of stainless steels**

Machinability refers to the difficulty of a material's machining, which cannot easily be expressed in quantitative terms, being instead used as a qualitative property [24], [25].

Generally, all grades of stainless steels (SS) feature difficult to cut behaviour due to their mechanical and thermal properties, which commonly consist of high temperatures, forces and wear rates, material adhesion on the tool and poor surface finish [26].

Among the existing grades of stainless steels, duplex and super duplex grades exhibit the more intense condition of temperature, forces and adhesion during machining. The main concerns of duplex and super duplex machining are [26]–[28]:

- High adhesive behaviour combined with mechanical strength and work hardening result in high cutting forces, which can lead to the chipping of the cutting tool.
- Low thermal conductivity and severe friction conditions promotes elevated cutting temperatures, causing the emergence of diffusion and oxidation tool wear mechanisms.
- Early tool failure and considerable surface damage as consequence of this severe processing.

## 2.3 – CUTTING TOOLS

Appropriate cutting tool selection is one of the main factors of a successful cutting operation where tool shape, material and coating need to be matched with the type of operation, workpiece material and cutting conditions [25]. The tools are under elevated compressive stresses during cutting (continuous and intermittent) and temperatures, and therefore need to possess enhanced hardness, fracture toughness, chemical and thermal stability, as well as fatigue resistance [26]. Considering the several cutting tool material options (HSS, carbide, ceramic, CBN and diamond), cemented carbide tools will be used in this work due to their widespread applications in industry and suitability for the process.

### 2.3.1 – Tool wear

Tool wear is inherent in the cutting process, where wear mechanisms and modes depend on the workpiece and tool material, as well as cutting conditions. One focus of metal cutting research is the development of cutting performance based on tool wear studies.

Stephenson and Agapiou [26] describe five different wear mechanisms: adhesive, abrasive, diffusion, oxidation and chemical wear.

- Adhesive wear is characterized by chip adhesion or welding to the tool due to the friction. Detached microscopic parts of the tool are carried away with the chip flow.
- Abrasive wear is caused by the interaction of hard particles present in the material with the cutting tool.
- Diffusion wear occurs when temperature and contact cause the tool material components to diffuse into the chip.
- Oxidation is the reaction between tool components (mainly binder) and atmospheric oxygen.
- Chemical wear is produced by chemical reactions between the tool and the workpiece present on both the flank and rake faces.

In addition to these five wear mechanisms, several other wear types can be associated with mechanical and thermal effects. Figure 7 illustrates some extra tool wear modes such as plastic deformation, thermal and mechanical cracks.

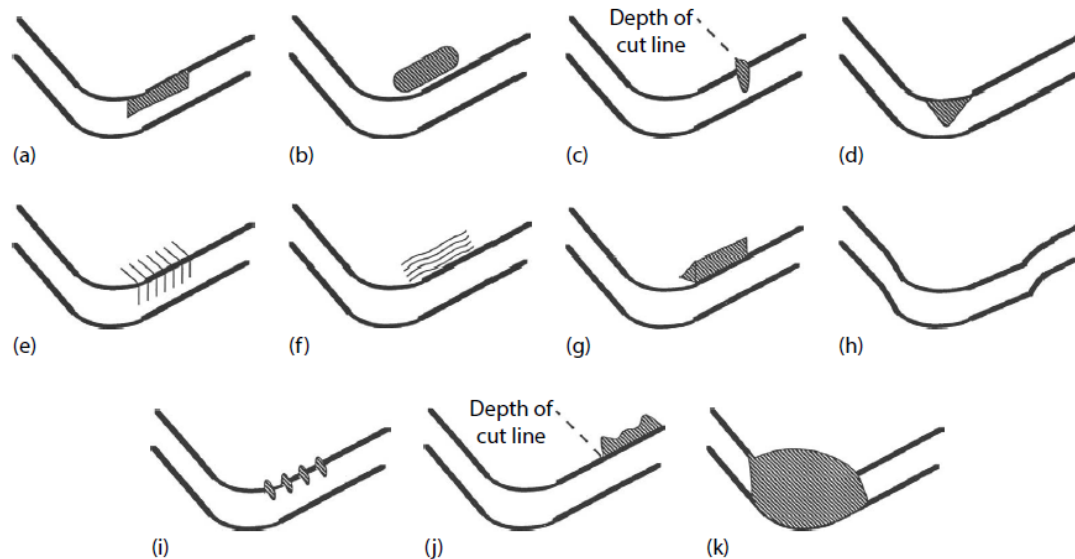


Figure 7: Tool wear types on cutting tools [reprinted from [19] with permission]:  
(a) flank wear; (b) crater wear; (c) notch wear; (d) nose radius; (e) thermal cracks;  
(f) mechanical cracks; (g) built-up edge; (h) plastic deformation; (i) edge chipping;  
(j) chip hammering; (k) gross fracture.

### 2.3.2 – Coating technologies

Cutting process conditions are highly unfavourable to the cutting tools, in which the process performance is directly related with their integrity. Among the current technologies focusing on process performance and tool life improvement, the application of coatings to the cutting tools is the most widespread. Its main objective is to deliver enhanced mechanical and thermal properties to the plain tooling substrate.

Deposition technologies can be separated into two distinct processes: Chemical Vapour Deposition and Physical Vapour Deposition. The PVD process

requires less temperature than CVD due to its ionisation method, where the atoms are attracted to the tool by the bias charge [24].

## 2.4 – SURFACE INTEGRITY AFTER MACHINING

The material selection for engineering components is driven by the bulk properties of the material having to meet the operational demands. For a range of applications however, the surface properties will control material behaviour by assuming different functions in complex environments. In these cases, the component performance is the result of the material surface characteristics, exposed area and environmental conditions [29].

The concept of surface integrity (SI) is given by the natural condition of a surface produced by machining and other surface processing techniques, where the process parameters contribute to the main surface characteristics. For example, a surface generated by rough turning will be different from a fine ground surface or a polished surface and so on. Surface integrity not only concerns topological aspects, but also mechanical, physical, metallurgical and biological ones as well. Among the abnormalities found on surfaces, the most common are plastic deformation, cracks and microcracks, work hardening effects, phase transformation, residual stresses and material tear [29].

### 2.4.1 – Surface topography and texture

This characteristic refers to the physical features of an area, which in SI is highly dependent on the tool used in the process, as well as machining conditions and the dynamic properties of the system. For example, use of a worn tool along with vibrations in the system will produce a different surface in rough turning than during finish turning with a new tool and a more rigid system [25], [29].

The surface texture characterization consists of the analysis of micro-geometric deviations, such as grooves, cracks and microfeatures without the influence or macro-geometric distortions such as waviness [29]. The most popular parameter of surface integrity assessment is the arithmetic average roughness  $R_a$ , which is widely used as a surface specification of manufactured parts. This parameter is derived from the arithmetic average of the deviations (peaks and valleys) about a profile centerline within a determined length, as shown in Figure 8. The higher the values, the rougher is the surface.

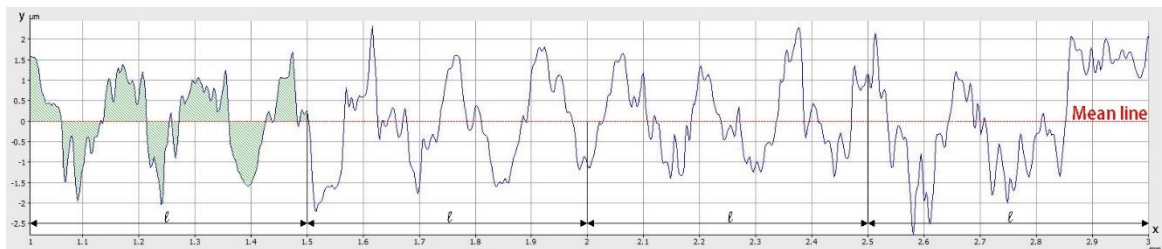


Figure 8: Arithmetic average roughness parameter  $R_a$  [based on [29]].

### **2.4.2 – Residual stresses**

Residual stresses are static triaxial stress states that are in equilibrium without any influence of external forces/momentums. These stresses are formed due to external and internal factors such as thermal and mechanical loads, phase transformations and diffusion processes that promote strain incompatibilities in the microstructure under conditions of volumetric equilibrium [29].

Tensile and compressive are the two different kinds of residual stresses, each having different effects on the manufactured part. Compressive stresses have a beneficial impact on the surface, as the superficial shrinkage prevents crack initiation and propagation, which is crucial to the component's fatigue strength. Conversely, due to their orientation the tensile residual stresses can easily nucleate and propagate cracks, which is undesirable for fatigue and stress corrosion applications [29].

The concept of acceptable component service life must be taken into consideration during the design stage. To achieve this, not only is proper material selection essential for the given work conditions, but also appropriate surface processing and material treatment to prevent detrimental aspects of residual stresses.

## 2.5 – CORROSION

Corrosion is an inherent aspect of any metal or metallic alloy, affecting everything from inexpensive household steel objects to massive industrial machinery. The well-known detrimental corrosion effects combined with severe operational conditions can catastrophically damage any functional component. Many industrial sectors such as chemical, oil and gas, aeronautical, construction and electric power generation are susceptible to corrosion effects to some degree. As such, the economic and safety consequences of corrosion need to be considered during the project stage and operation. The costs associated with corrosion go beyond than just maintenance and prevention. Negligence can result in the loss of efficiency, contamination, plant downtime, higher maintenance costs, as well as serious risks to the environment and health. Corrosion failures of high-pressure boilers, nuclear reactors and oil pipelines demonstrate the importance of corrosion prevention.

Several major characteristics of corrosion are outlined, followed by corrosion mechanisms and aspects that specifically concern stainless steels.

### 2.5.1 – Definitions

Corrosion is a destructive chemical reaction between a metal or alloy and the environment. These reactions revert the metal atoms to their natural state, which then become bonded to other chemical compounds, forming products that are similar or even identical to their original mineral form [30].

In almost all corrosion processes of metals dissolved in aqueous solutions, electron transfer occurs between two parts. The following expression illustrates the reaction mechanism between metallic zinc (Zn) and hydrochloric acid:



Since it is an acid solution, the two molecules of HCl are in the ionic form of  $2H^+$  and  $2Cl^-$ , zinc reacts with this solution by releasing two electrons that are absorbed by the two  $H^+$  atoms, forming  $H_2$  gas. At the same time, zinc assumes a new valence of  $Zn^{+2}$ , remaining in its ionic form within the solution. Equation 3 expresses the oxidation of zinc, whose valence increases from 0 to +2. This is known as an anodic reaction where  $e^-$  represents the electron.



Equation 4 shows the cathodic reaction of a hydrogen ion in combination with two electrons from zinc. The hydrogen valence decreases from +1 to 0. Both Equations 3 and 4 are also known as half-cell reactions since together they represent the full electrochemical reaction:



The ionic solution carries the flow of ions from the anode to the cathode completing the electrochemical system. All corrosion reactions in aqueous environments, either in liquid or vapour form, are considered to be electrochemical reactions. Without the presence of water, only corrosion reactions where transfers of electrons occurs are also considered electrochemical [30].

### **2.5.2 – Polarization and passivity**

To gain a better understanding of the corrosion mechanisms, two concepts must be illustrated. The concept of polarization is used in experimental procedures to enable detailed studies of active-passive behaviour of materials, as well as passive film formation and growth [30].

The polarization mechanism is given by the change in the half-cell equilibrium potential. Depending on its direction, polarization will promote an abundance or lack of electrons in the reactive surface, increasing the tendency of

one half-cell reaction over the other. In the previous zinc and hydrochloric acid reaction, if more electrons are made available on the zinc surface, the potential will drop from the equilibrium and promote the cathodic reaction, consequently slowing the anodic reaction rate, which is known as cathodic polarization. The opposite is also true. If the surface potential is positively higher than the equilibrium due to a lack of electrons, the tendency of anodic dissolution will increase due to the anodic polarization [30].

During the corrosion process, both cathodic and anodic half-cell reactions co-occur on the conductive surface where each reaction has its electric potential. In an equilibrium state, no potential is predominant over the other. Instead, there is one common intermediate potential called the corrosion potential ( $E_{corr}$ ) [30].

The concept of passivity is the decrease in the corrosion rate (corrosion resistance) after a given potential ( $E_P$ ), even in the presence of a high corrosive driving force (anodic polarization). Many metals and alloys can exhibit this type of passivation, followed by a considerable reduction in the corrosion rate. This behaviour is caused by the formation of thin protective hydrated oxide films on the surface as a consequence of the corrosion process, who act as a barrier that slows down the anodic dissolution. Elements such as Cr and Ni enhance passivation in stainless steels. The passivation of an alloy, is highly dependent on the oxidation power of the solution, where the alloy can be in its active state below the critical potential or in its passive state above the critical potential [30]. Figure 9 summarizes these concepts in a polarization chart.

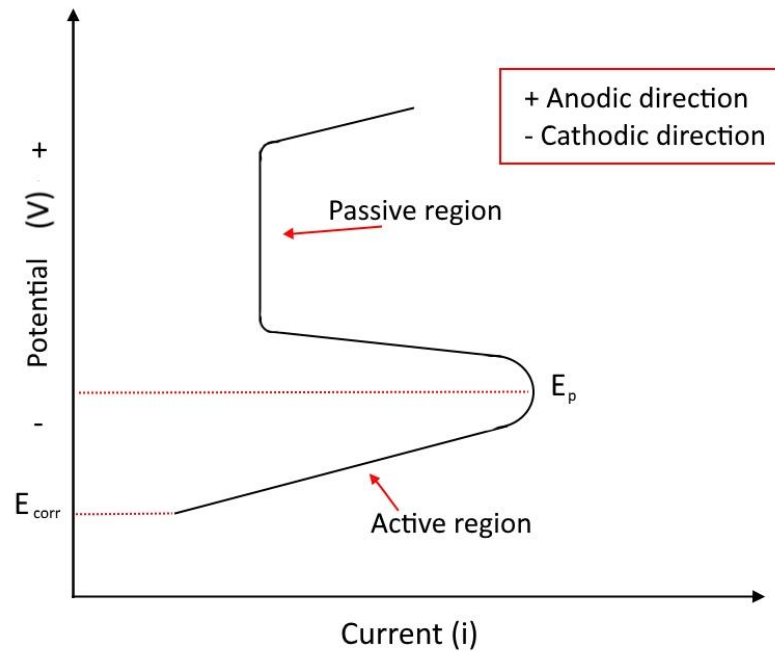


Figure 9: Typical polarization curve [based on [30]].

### 2.5.3 – Corrosion of super duplex stainless steel

The superior corrosion resistance of super duplex stainless steel is already well-known to be a result of its chemical composition and microstructure. However, even with its superior properties, the alloy is still susceptible to corrosion, mainly by pitting and stress corrosion cracking [5],[3],[7].

Pitting is a localised form of corrosion with rapid penetration within small and discrete areas. In stainless alloys, this type of corrosion tends to occur in neutral to acidic pH as well as chloride-rich environments, where the pitting corrosion susceptibility increases when the temperature also increases. A failure in the

passive film protecting the surface at isolated sites causes the emergence of this type of corrosion, which tends to be unpredictable and hard to detect due to the presence of pits covered by insoluble corrosion products. Pitting occurs on an exposed surface, where a small volume of solution is enclosed in the pit geometry after a cavity is formed, which promotes localized acidification and consequently a higher corrosion rate [30]. Figure 10 shows the effects of pitting corrosion on a surface.

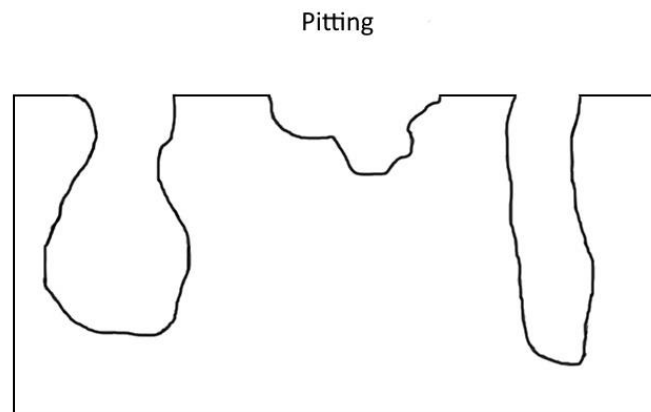


Figure 10: Typical pitting corrosion geometry [based on [30]].

The material undergoing stress corrosion cracking (SCC) has brittle characteristics at a relatively low tensile stress applied to the component exposed to a corrosive environment. In case of stainless steel, hot and chloride rich solutions promote cracks on the material surface. The applied stresses do not have to be highly intense to develop stress corrosion cracking but will only require a longer time to reach failure. Assembly misalignments and uneven thermal

expansion/contraction are examples of low-intensity stresses that can cause SCC. The cracks can propagate through the grains (transgranular) or even in between grains (intergranular), as shown in Figure 11, always normal to the tensile component. The electrochemical potential plays a slightly different role in SCC than in pitting type of corrosion. While a passive film is necessary for SCC to occur, it is more likely in potentials that destabilize the film. In many cases, although not mandatory, corrosion pits on the surface can act as starting points for SCC [30].

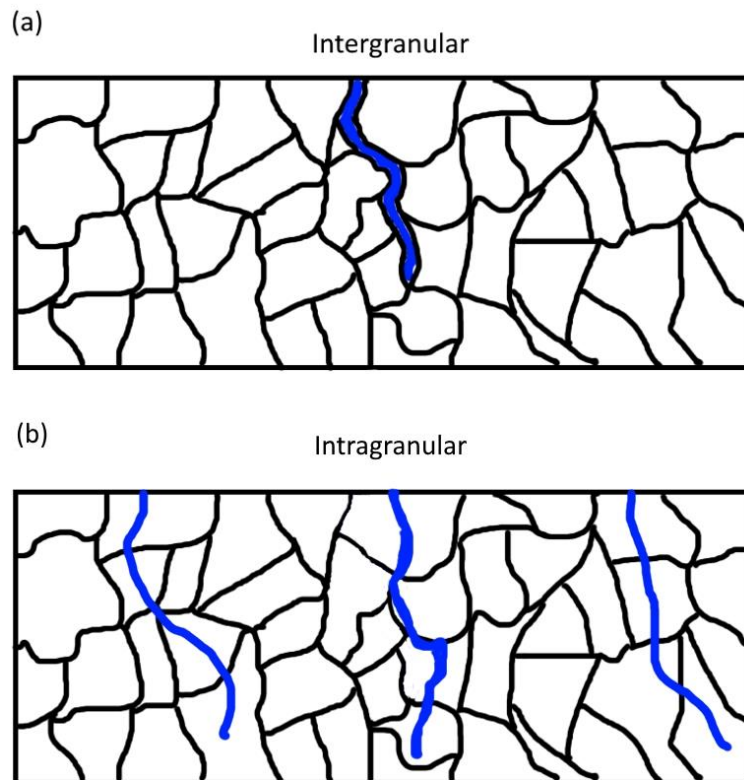


Figure 11: Intergranular (a) and transgranular (b) stress corrosion cracking propagation diagram [based on [30]].

The theoretical base presented in this chapter illustrated that major characteristics of SDSS are a result of its microstructure and high alloy content, which has an impact on the machining process characteristics, surface integrity and its functional performance/corrosion resistance. The proposed method of studying the effects of PVD coated tools on the machining performance and corrosion of SDSS is detailed in the next chapter.

## 2.6 – STATE OF THE ART

The great concern regarding corrosion of SDSS is the detrimental effects of the secondary phases in terms of localized corrosion. The current studies investigated the degradation of corrosion resistance and mechanical properties of SDSS due the induced formation of detrimental secondary phases by different thermal treatments [9], [23], [31], [32].

Welding of SDSS is a common operation for part of chemical and petrochemical machinery. However, proper microstructure control is quite difficult for this operation since the material goes through rapid heating and cooling process, favouring formation of deleterious phases. Different studies were performed regarding the welding effects in the microstructure, corrosion resistance and mechanical properties [19], [22], [33], [34]. SCC was also studied in welding joints at low strain by Tavares et al. [13].

Machining of SDSS is also a common industrial operation. Królczyk et al. [35] performed a general machinability study of two different commercial carbide coatings during machining of SDSS at different cutting conditions. Paiva et al. [28] studied the performance of three different coated tools at fixed industrial cutting conditions where a deeper coating analysis was performed. Both on them analyzed the material microstructure after cutting. Bordinassi et al. [36] studied the effect of different cutting conditions on the SDSS surface integrity in terms of surface roughness, residual stresses and microstructural modifications.

Two different studies show the effect of machining in the corrosion of SDSS. The first study, done by Oliveira et al. [37], consisted in analyze the pitting density after machining using different cutting speeds and coolant pressure. While Rajaguru et al. [3] studied the SCC susceptibility of SDSS after tensile residual stresses being induced by a machining process without the use of any kind of cooling method.

This research is a complement to the previous ones here described, since the role of different PVD coatings applied to the cutting tools was not yet related with the corrosion and SCC susceptibility of SDSS.

### **CHAPTER 3 – METHODOLOGY**

The experimental methodology used in this study is presented in this chapter. A schematic model outlining the steps of the experimental procedure is shown in Figure 12. The first step was the workpiece characterization, where the material microstructure was analysed. The second step consisted of the machining test, where tool life data, cutting force measurements and wear analysis were conducted. Surface integrity studies were carried out on the machined surface produced by each cutting tool, in which surface texture, hardness measurements and residual stresses were evaluated. The final stage was a study of surface corrosion susceptibility via polarization measurements followed by a stress cracking corrosion specific test. Based on results of tool life, cutting forces and residual stresses, additional X-ray photoelectron spectroscopy was performed to analyze the chemical and microstructural transformations on AlTiN and AlCrN/TiSiN tools.

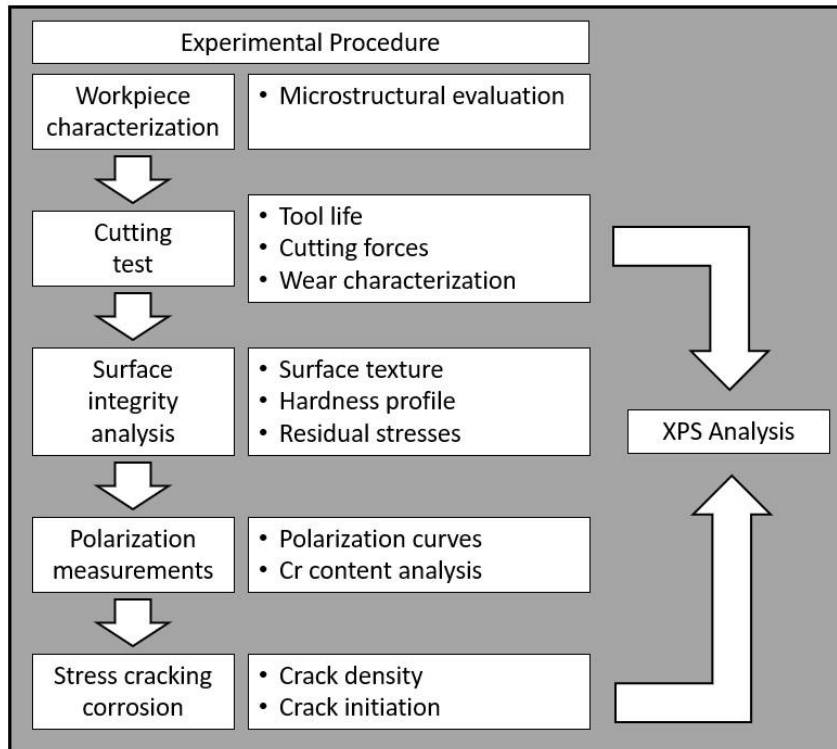


Figure 12: Experimental plan schematics.

### 3.1 – WORKPIECE CHARACTERIZATION

The tube stock material used in these studies was a super duplex stainless steel UNS S32750 produced by V&M Tubes Solutions of Brazil. The material chemical compositions provided by the manufacturer are displayed in table 4.

Table 4: Chemical composition of UNS S32750 tubes (V&M Tubes).

| Element | C    | Cr    | Ni     | Mn     | Si    | Mo   | P     | Cu     | S     | W    |
|---------|------|-------|--------|--------|-------|------|-------|--------|-------|------|
| Wt. (%) | 0.03 | 25.0  | 7.12   | 1.13   | 0.65  | 4.0  | 0.029 | 0.78   | 0.018 | 0.61 |
| Element | N    | Zr    | Nb     | Al     | Co    | V    | Ti    | Pb     | Sn    | Fe   |
| Wt. (%) | 0.30 | 0.047 | <0.001 | <0.001 | 0.045 | 0.06 | 0.005 | 0.0012 | 0.086 | Bal  |

It is possible to input the chemical element content into Equation 1 to estimate the pitting resistance equivalent number of the alloy. This input will result in:

$$\text{PREN} = \%Cr + 3.3\%Mo + 16\%N$$

$$\text{PREN} = 25.0 + 3.3 \cdot 4.0 + 16 \cdot 0.3$$

$$\text{PREN} = 43$$

To analyse SDSS microstructure a sample cross-section was cut parallel to the axial direction of the tube (extrusion direction), mounted in epoxy resin and metallographically prepared using conventional methods and etched in a solution composed of 50 ml of HCl (50% v/v) + 10 ml of ethanol (C<sub>2</sub>H<sub>5</sub>OH) to differentiate each phase. An optical microscope Keyence VHX-6000 was used to collect microstructural images. The ratio of each phase was calculated using the image processing software ImageJ. Figure 13 shows the material microstructure. The SDSS microstructure on the analysed area was composed of 49% austenite and 51% ferrite.

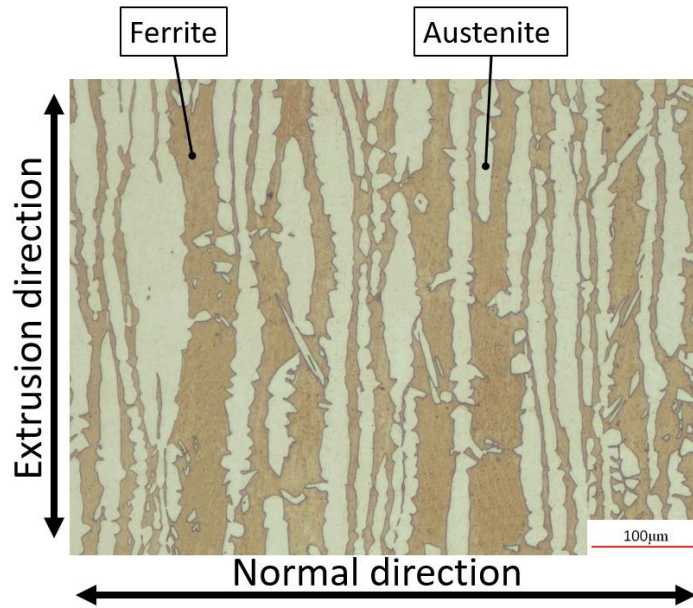


Figure 13: UNS S32750 microstructure.

### 3.2 – CUTTING TESTS

Cutting tests were performed by a turning operation on a Nakamura-Tome SC-450 CNC turning machine under the following cutting conditions: (i) cutting speed: 120 m/min; (ii) feed rate: 0.15 mm/rev; (iii) depth of cut: 0.5 mm; (iv) coolant flow rate: 10 L/min.

A tubular SDSS geometry was chosen according to the dimensions in Figure 14 due to be the same shape being used in industry, wherever it was possible to replicate similar clamping and dynamic conditions.

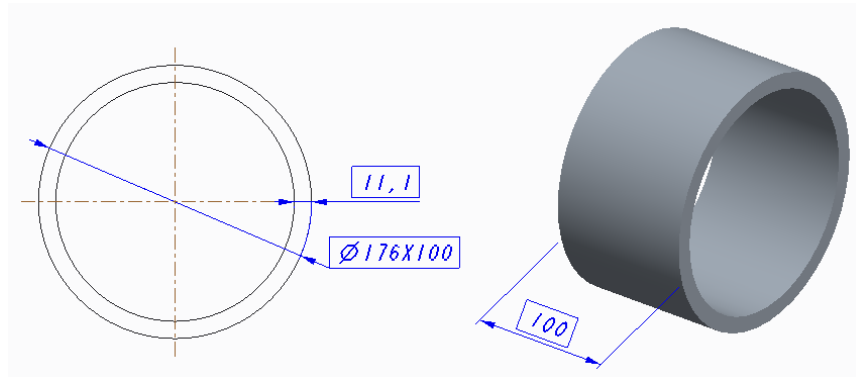


Figure 14: Workpiece shape and dimensions.

Cutting forces were collected for the first 50 meters of cutting length using a Kistler 9121 type quartz 3-component force ( $F_x$ ,  $F_y$ ,  $F_z$ ) dynamometer with maximum measuring ranges of -3 kN to 3 kN on X and Y direction and -4 kN to 4 kN on Z direction. The natural frequency of the system was 10 kHz. A National Instrument NI 9125 DAQ board was used for data acquisition, with a total resolution of 16-bit, a voltage of  $\pm 10$  V and sampling rate of 5 kHz. The signal was amplified by a Kistler 5010 amplifier with a maximum voltage of 50 V.

Sandvik CNMG120408-SM-H13A finishing inserts were selected for the tests using three different PVD coatings commercially deposited by Oerlikon-Balzers. Coating composition and architecture are presented in Table 5.

Table 5: PVD coatings composition and architecture.

| Coating     | Composition  | Architecture |
|-------------|--|--------------|
| AlCrN/TiSiN | Al <sub>50</sub> Cr <sub>50</sub> N/Ti <sub>95</sub> Si <sub>5</sub> N | Multilayer   |
| AlCrN       | Al <sub>50</sub> Cr <sub>50</sub> N                                    | Monolayer    |
| AlTiN       | Al <sub>67</sub> Ti <sub>33</sub> N                                    | Monolayer    |

The same multilayer coating as used in industry was selected as a benchmark. The other two monolayer coatings were selected from literature due to their solid machining performance and oxidation resistance.

The tool-life criteria were either an average flank wear/chipping of 300  $\mu\text{m}$ , as described by ISO 3685, or a total cutting length of 3000 meters (maximum tool life achieved in industry). The tool flank wear assessment was performed on a Mitutoyo Toolmaker optical microscope equipped with digital micrometre heads. Following the cutting tests, the wear was characterized by a Tescan Vega II scanning electron microscope (SEM).

In addition to wear characterization, X-ray Photoelectron Spectroscopy (XPS) was performed for AlTiN and AlCrN/TiSiN tools on the rake face to determine any structural or phase transformation during the cutting. The analysis was carried on a Physical Electronics Quantera II equipment with hemispherical Al anode source and quartz crystal monochromator to focus the X-rays. The operating pressure was around  $1 \times 10^{-9}$  Torr, where the samples were sputter-cleaned for 5 minutes each and the beam size used on the analysis was 55  $\mu\text{m}$  for AlTiN and 110  $\mu\text{m}$  AlCrN/TiSiN.

### 3.3 – SURFACE INTEGRITY

To assess surface integrity following the cutting tests, three different characterizations were performed: surface texture, hardness profile and residual stresses measurement. Each kind of characterization is explained in detail in the following topics.

#### **3.3.1 – Surface texture**

After machining experiments, surfaces produced by each PVD tool were preserved and sectioned into smaller samples by waterjet cutting. Each coupon sample was cleaned in an ultrasonic bath with ethanol for 280 seconds and then scanned by a white light spectroscopy Alicona Infinite Focus optical microscope equipped with focus variation technology. A random selected area of 1 mm<sup>2</sup> of each sample was scanned with the 100x lenses. Form corrections were later applied to neutralise the influence of the workpiece cylindrical shape, resulting only in the surface profile. After corrections were made, the surface texture was computed by the built-in surface texture module.

### **3.3.2 – Hardness profile**

Another set of coupon samples were mounted in epoxy resin and metallographically prepared by conventional methods until a mirror-polished surface was reached, followed by etching using the same reagent as described in item 3.1. After etching, the samples were taken to microhardness analysis on a Matsuzawa model MMT-X hardness tester using a Vickers indenter. Loads of 10 g were applied for 10 seconds. The matrix had a total of 21 points divided into seven lines and three columns, where the measurements started at 15 microns from the machined surface, with a spacing of 30 microns present between each indentation. The only exception was for the AlCrN/TiSiN coated tool, since it presented a deeper work hardening effect.

### **3.3.3 – Residual stresses**

Residual stresses on the machined surface were measured by X-ray diffractometry method on an LXRD diffractometer using Mn and Cr targets to respectively analyse the austenitic and ferritic phase. The diffraction of austenite was observed in the {311} plane with a Bragg Angle ( $2\theta$ ) of 152.8 degrees and the ferrite diffraction in plane {211} with 156.4 degrees. A total of 20 measurements were done for each sample in directions parallel (cutting direction) and orthogonal (feed direction) to the tool grooves as shown by Figure 15. To assess the

machining effect on the material surface, a mirror-polished SDSS sample was used as a benchmark for this analysis.

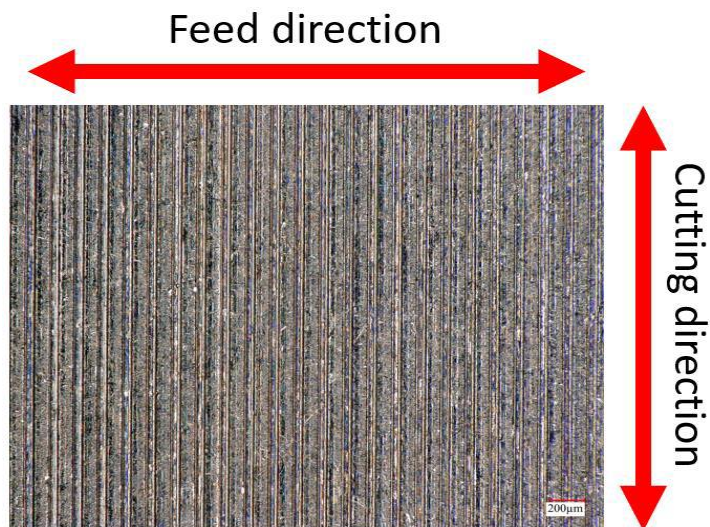


Figure 15: Cutting and feed direction of SDSS machined sample.

### 3.4 – CORROSION TESTS

Two different corrosion tests were performed to assess the material behaviour after machining; a set of potentiodynamic anodic polarization measurements compared the corrosion susceptibility of the surfaces and a specific stress cracking corrosion experiment correlated the surface integrity state of each sample with SCC. The benchmark surface in both tests was a mirror-polished SDSS sample, as discussed in item 3.3.3.

### 3.4.1 – Potentiodynamic anodic polarizations

Coupons composed of each machined surface were prepared as working electrodes in the polarization cell by being wired on the face opposite to machining and coated with epoxy resin and PTFE tape, so that only the machined surface was exposed to the environment. The reactive area of each sample was calculated on a Keyence VHX-5000 optical microscope. The polarization measurements were performed by a computer-controlled PAR EG&G Model 270 Potentiostat, as described by ASTM G5, where a saturated calomel (KCl) electrode was used as a reference and carbon rods served as counter electrodes. The electrolytic solution used in this study had a total of 1 litre in volume composed by deionised water, 1 mol of sodium chloride (NaCl) and 1 mol of sulphuric acid (H<sub>2</sub>SO<sub>4</sub>) at 90 °C heated by a hot plate with feedback control. A calibrated thermometer was used to calibrate the hot plate feedback control. Solution deoxidation was done with humid nitrogen gas (N<sub>2</sub>) for two hours. Once the temperature was achieved and deoxidation was completed, the sample was inserted into the cell on an open circuit until the potential was stabilised for at least 1000 seconds. The samples were polarized from -0.3 V<sub>SCE</sub> to 1.3 V<sub>SCE</sub> about corrosion potential at a scanning rate of 1 mV/s. A set of three samples of each surface was tested for reproducibility. The electrolytic cell setup as described is displayed in Figure 16(a), while Figure 16(b) shows the sample preparation technique.

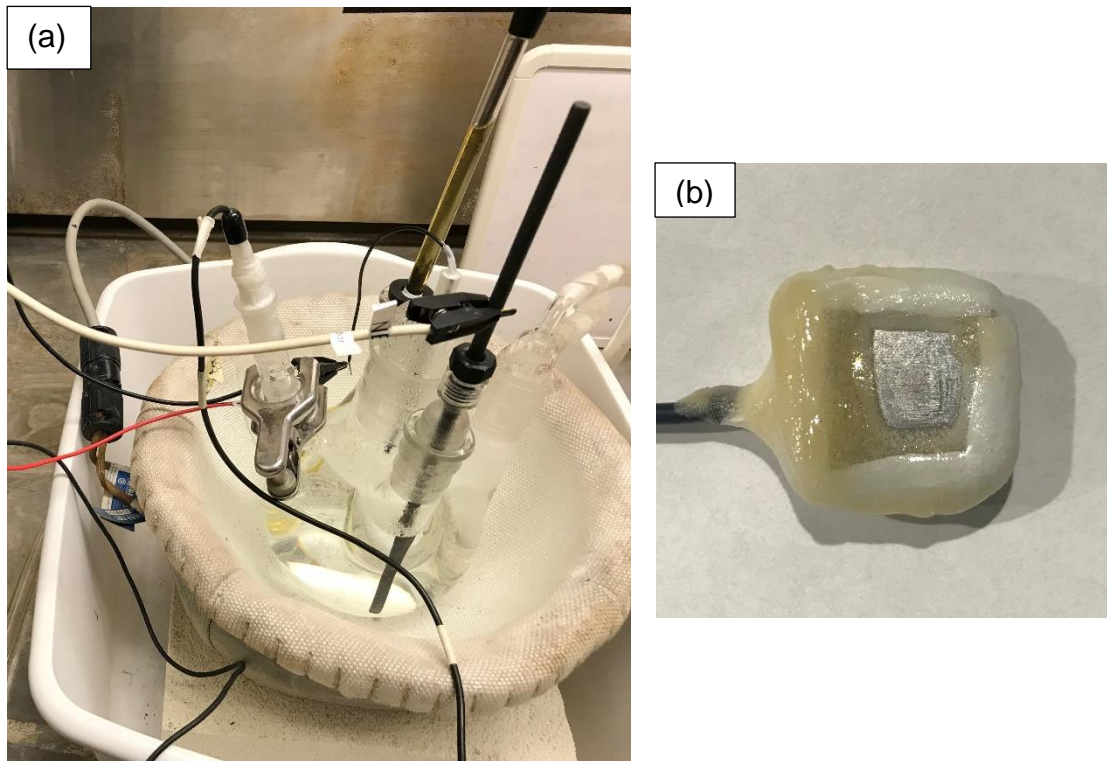


Figure 16: Electrolytic cell setup (a) and sample (b) used in the polarization measurements.

To complement the polarization measurements a Cr content profile was done on the machined layer. A JEOL JAMP-9500F FE-Auger microscope was used to alternate between EDS analysis and sputtering material away, creating a profile orthogonal to the machined surface. Besides sputtering capability, the auger microscope was chosen due to its high special resolutions.

### **3.4.2 – Stress cracking corrosion**

The stress corrosion cracking experiment was conducted following an ASTM G36 standard, where a 400 mL solution of hexahydrate magnesium chloride was prepared using 600 g of reagent grade  $\text{MgCl}_2 \cdot 6\text{H}_2\text{O}$  and 15 mL of reagent water. A hot plate with temperature feedback was used to heat and keep the solution at a boiling point. After the boiling point was reached, the temperature was adjusted to  $155^\circ\text{C}$  by adding water drops to the solution. A condenser was attached to the cell to prevent excessive water evaporation and consequently, drastic changes in concentration and temperature. To guarantee the correct temperature of the system, a thermometer was assembled in the cell, which was continuously checked during the test. Samples of around  $1\text{ cm}^2$  were cut from different parts of the machined piece, reaching a total of nine samples, corresponding to 3 samples of each machined surface plus an extra set of 3 mirror polished SDSS samples to serve as benchmarks. The samples were held in a PTFE holder and the total test was carried out in 2 hours. Following its conclusion, samples were cooled, cleaned and the surface of interest was inspected by scanning electron microscopy. A total of 20 images were randomly taken from an area of  $0.5\text{ cm}^2$  of each test sample in order to average the surface state. Crack lengths were calculated using NeuronJ, an add-on of ImageJ software. This add-on detected the different colour scales between the cracks and the surface, which is an easy way to calculate the lengths. The results are displayed in terms of crack density, which is the total crack lengths

by unit of area. Later, cross-sections of each kind of samples, were metallographically prepared in every direction and etched as described in section 3.1 to analyse the nucleation of the cracks.

## **CHAPTER 4 – RESULTS AND DISCUSSION**

In this chapter the results achieved are presented based on the experimental plan shown by Figure 12. The discussion will begin with the cutting tests results, followed by surface integrity studies. These two first topics are then correlated with the corrosion tests results.

### **4.1 – CUTTING TESTS**

Tool life performance and the wear mechanisms of three coated inserts were assessed through turning operations under finishing conditions described in section 3.2. Life curves of the selected inserts are displayed in Figure 17.

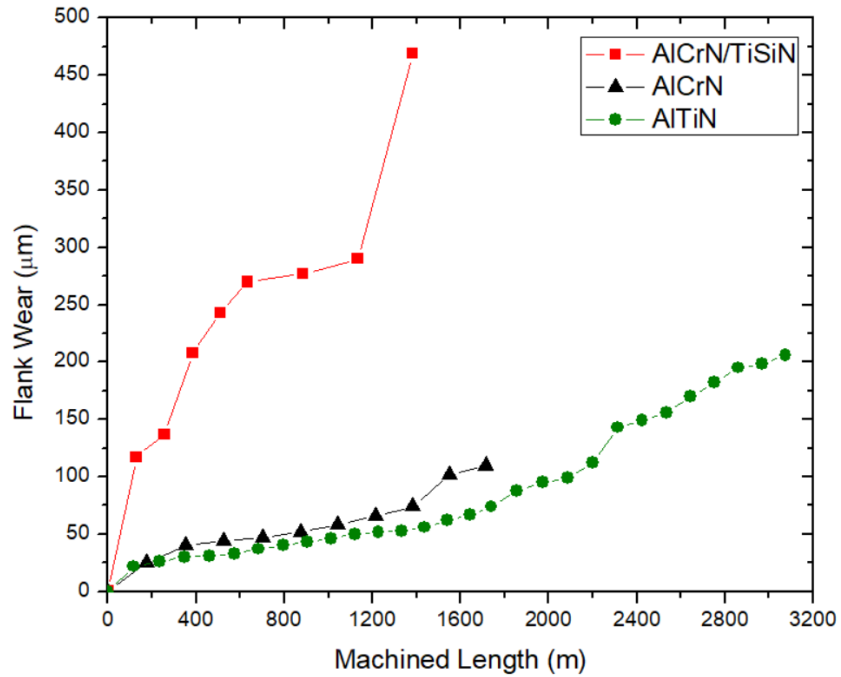


Figure 17: Tool life results given by flank wear versus cutting length.

This figure shows that AlCrN/TiSiN and AlCrN coated tools performed worse than AlTiN, which featured nearly the double the life of the other two tools. Scanning electron microscopy images are shown in Figure 18 to analyse the wear mechanisms acting on the cutting tool.

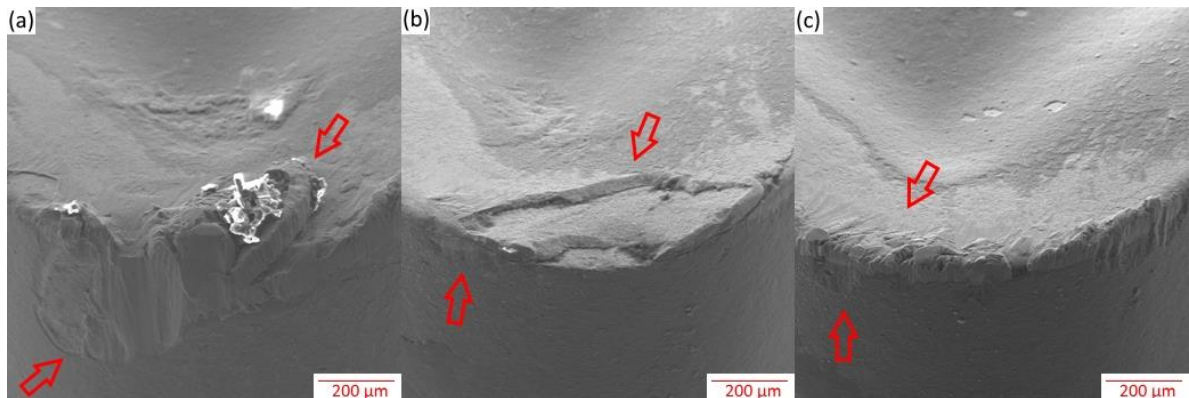


Figure 18: Worn turning tools SEM analysis: (a) AICrN/TiSiN, (b) AICrN and (c) AlTiN.

As shown in Figure 18 (a) and (b), major tool failure mechanisms are chipping in the multilayer tool and coating delamination in AICrN. Built-up edge (BUE) formation, as well as chipping is easily visible in Figure 18 (a), whereas in Figure (b) it is possible to see the tool corner with the delaminated coating. In Figure (c) the BUE is smaller compared to that of the tool with a multilayer coating. BUE also covers the traces of abrasive flank wear right beneath the cutting edge.

Due to its ductile nature, SDSS machining results in a high amount of material adhering to the tool surface, which generates BUE [38]. This bond is strong enough to continue growing throughout the cutting process until it becomes unstable and breaks away, carrying a part of the tool along with it [25], [26]. This behaviour was the failure mechanism of AICrN/TiSiN and AICrN tools. Similar phenomena were also described by Nomani et al. In their study, the main wear mechanisms observed on the tool during the machining of super duplex 2507 were adhesion and abrasion [39]. The presence of workpiece material on the surface of

cutting tools confirms that adhesion is the predominant wear mode in this operation. Out of the tested tools, it is least severe in the one coated with AlTiN.

The good performance of AlTiN tools may be attributed to its ability to self-adapt to the process conditions, forming nanometric structures that improve the tribological conditions at the tool-chip interface. These secondary structures are usually called tribofilms and the coatings that produce these types of surface films are known as adaptative coatings. Such films are the result of tribo-oxidation that happens during the cutting process, where elevated temperatures and pressures are required to initialize the chemical transformation. Heat generated during the process plays a critical role in the formation and the constant regeneration of such surface structures [40].

Paiva et al. (2017) performed similar wear studies on the same AlTiN coating composition. It was reported in their study that this aluminium-rich coating undergoes tribo-oxidation and forms a surface aluminium oxide with nanometer thin alumina ( $\text{Al}_2\text{O}_3$ ) structure on the rake surface of the tool. This oxide has a ceramic nature that alters the wear performance of the cutting tool. These films create a thermal-barrier effect, which prevents heat penetration within the tool, thus minimising the tool wear [41]. The aluminium oxide formation is confirmed by the XPS results obtained, as displayed in Figure 19. The high resolution Al2s peak spectra shows a 100% of aluminium oxidation from the coating into beneficial  $\text{Al}_2\text{O}_3$  on the tool rake face at a binding energy of 118.9 eV. The thickness of the formed

film is around 9 nm. The oxidation of Ti in the full spectra shows the formation of non-protective Ti-O species in lower amount [28].

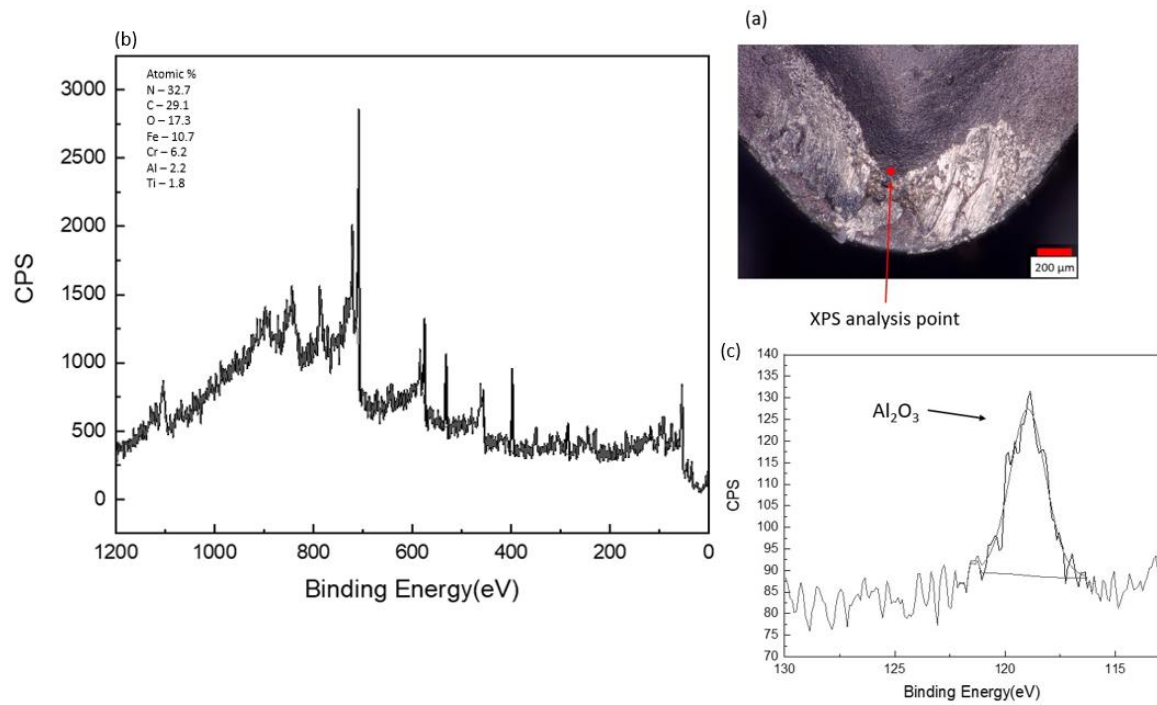


Figure 19: AlTiN coated tool XPS analysis (a) point selected for the analysis on the tool's rake face (b) full XPS spectra and (c) high resolution Al2s peak XPS spectra.

In addition to tool life curves and wear mechanism evaluation, the cutting force data shown in Figure 20 is also the part of the machining studies.

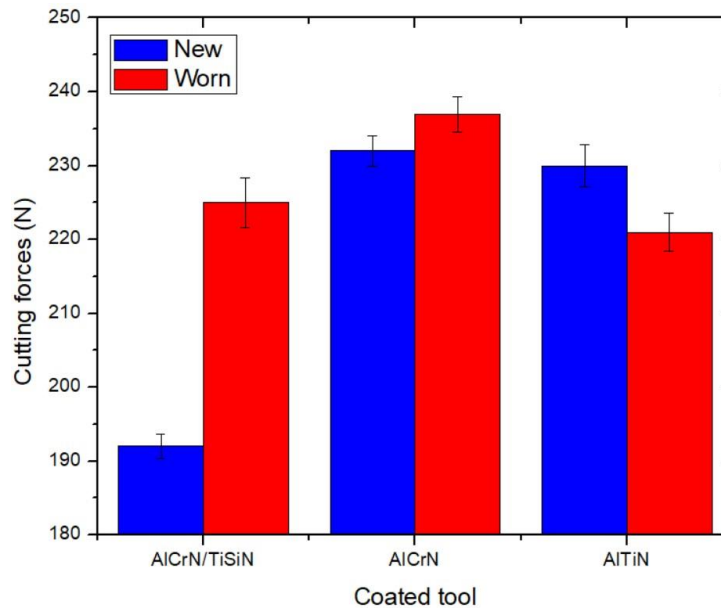


Figure 20: Acquired cutting forces versus tool life stage.

The cutting forces data show that the tool with a multilayer coating featured the lowest cutting forces. In comparison, the cutting force values for the AlCrN coated tool were the highest and those for the AlTiN coated tool in the middle of the three. However, the measurements of the worn condition reveal that the cutting forces decreased in the AlTiN coated tool, until they became less than those of the other two tools. After the cutting was complete, the AlCrN coating featured the highest cutting force values and those of the AlCrN/TiSiN coating were in between. As described by Felice et al., the cutting forces are the result of the existing friction between the tool and the workpiece material. Therefore, there is less friction in the AlTiN worn tool than in the others [42].

The low cutting forces of the new tool with a multilayer coating can be attributed to the low interaction of the coating with SDSS, which is confirmed by

the friction coefficient data obtained by Paiva et al. [27]. In their study, the tribological behaviour of similar compositions of AlCrN/TiSiN and AlCrN coatings as the ones used in this work were evaluated during the machining of the same SDSS grade. A pin-on-disc test showed that the multilayer coating had the lowest friction coefficient among all the tested coatings, which may account for the low cutting force values [27]. However, the temperatures and pressures in actual machining are much higher than those of a pin-on-disc test. For this reason, it is possible to account for the adhesion of the material to the tool surface in the multilayer coating, as well as the cutting force increase, a trend inherent to the process.

Considering the results of the previous tribological study [27] and the nature of the process, the AlCrN coated tool features expected behaviour. The high cutting forces are the result of a higher friction coefficient compared to the multilayer AlCrN/TiSiN, in which the increase of forces in the worn tool is inherent to the cutting process.

In contrast with the previous tools, the tool with the AlTiN coating had lower cutting forces under the worn condition. These low forces are another indication of the improvement in friction conditions provided by the adaptive behaviour of the coating due to the tribofilm formation.

## 4.2 – SURFACE INTEGRITY

The surface texture analysis results after the machining of each coated tool are displayed in Figure 21.

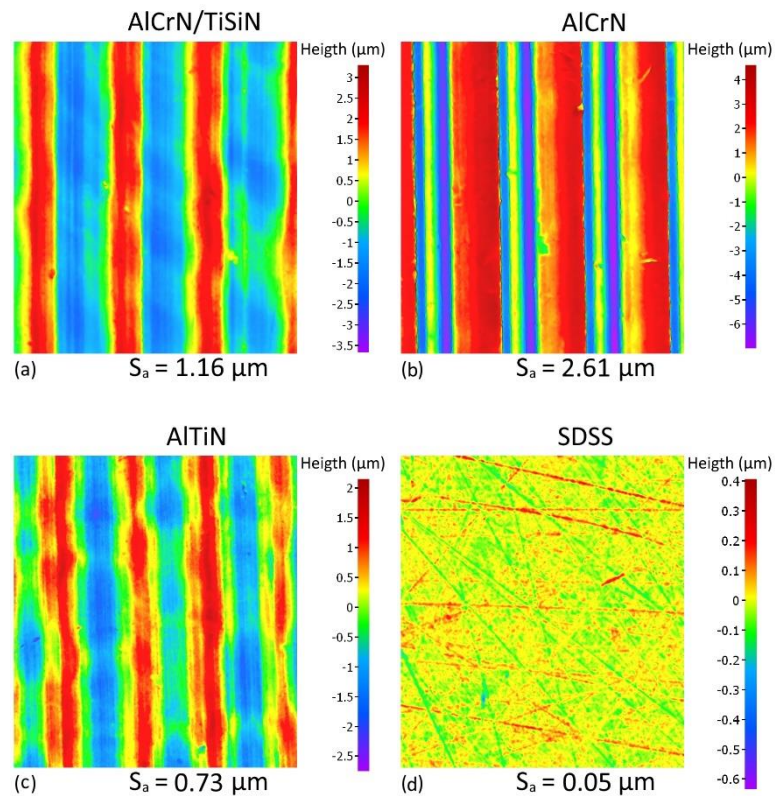


Figure 21: Surface texture produced with (a) AICrN/TiSiN, (b) AICrN, (c) AlTiN PVD coated tools and (d) mirror polished SDSS sample.

Surface texture data revealed that the AlTiN coated tool produced the smoothest surface out of the tested tools, followed by the multilayer tool and the AICrN coated tool, which had the roughest values. The benchmark surface showed very low roughness values compared to the machined surface due to its fine

polishing. The feed rate and tool nose radius are the factors affecting surface roughness the most [25]. Since these two aspects were kept constant, the differences in the machined surface textures among the tested tools must, therefore have had another cause.

Significant differences in groove height among the scanned surfaces can be observed in Figure 21, which are visible by colour scale. This difference can be attributed to the varying friction, system vibrations and tool condition and cutting-edge geometry of each tool.

The wear and adhesion of each tool results in a non-uniform cut, where the way that the volume of material that is plastically deformed before the shearing is not the same for all the tools, influenced by the geometry of cutting edge and rake face. The AlTiN coated tool had the least material adhesion/wear among all the tools and produced the best surface finish. The BUE structure on the tool with a multilayer coating increased the cutting-edge radius, thereby enhancing the ploughing effects, which resulted in an intermediate finish. Finally, the delaminated edge of the AlCrN tool developed a geometrical distortion on the tool that produced a rougher surface texture.

In addition to that, the difference in friction among the tools results in difference in chip flow resistance, where due to the continuous cut a difficult flow can have a small interference in the cutting region.

Besides the good clamping of workpiece and high rigidity of the tool fixture, vibrations are an aspect inherent of all machining process, which also contributes

to the surface finishing. It is important to note that the difference in the total depth range of the analysed surfaces is considerably small, not exceeding 10  $\mu\text{m}$ .

In this study a direct relation can be draw between the surface finish with the cutting forces measured for each coated tool, where higher friction will result in rougher surfaces. Chen concluded that materials with a more ductile behaviour tends to present a worst surface finishing than harder materials. He also states that there is a optimum value of flank wear that improves the surface finishing however, the radial thrust force is sensitive to the tool wear [43].

The plastic deformation effect can be seen in the microhardness profile of the machined surface presented in Figure 22.

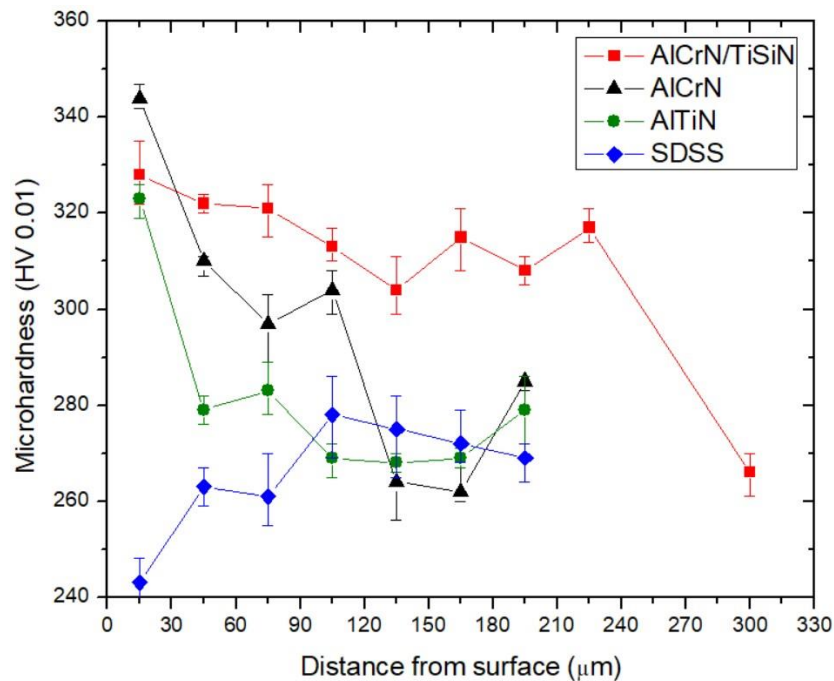


Figure 22: Microhardness profile of AlCrN, AlCrN/TiSiN, AlTiN and SDSS samples.

The microhardness profile results demonstrate the work hardening effect of each tool on the workpiece material subsurface. This profile corresponds with the cutting force and surface texture results, where the higher cutting forces of the AlCrN tool is a result of higher friction, which caused intensive plastic deformation and subsequent work hardening effect on the machined layer. Similar cutting force values in the multilayer and AlTiN coated tools resulted in similar superficial hardness levels. After the first measurement line, the hardness of AlTiN coated tool machined surface dropped to values close to the benchmark line (260-280 HV). The AlCrN presented a deeper work harden layer, where the hardness dropped to 260 HV around 135  $\mu\text{m}$ . Besides not presenting the higher hardness values on the surface, the multilayer coated tool machined surface had the wider work harden layer, where the benchmark hardness line was reached just between 225 and 300  $\mu\text{m}$ . The benchmark sample did not show such a significant difference in its profile as the machined samples, which indicates the strong effect of the cutting process on surface integrity.

The final surface integrity analysis and the residual stress measurements are displayed in Figure 23.

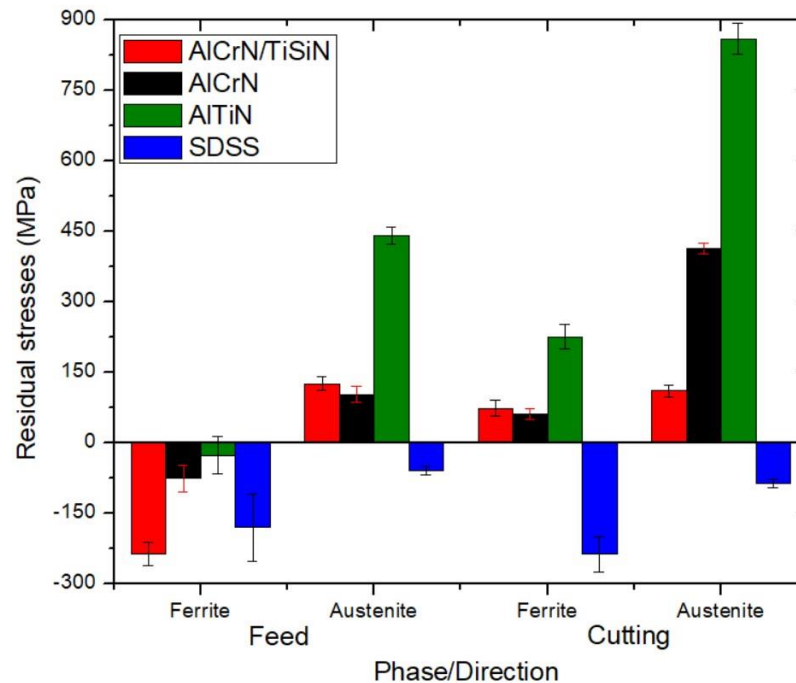


Figure 23: Residual stress measurements of AlCrN, AlCrN/TiSiN, AlTiN and SDSS samples.

Residual stress measurement results show that the ferritic phase had lower residual stresses than the austenitic phase in the same measurement direction. All tools had tensile residual stresses in both phases in the cutting direction, as well as in the austenitic phase in the feed direction. The exception was in the ferrite phase in the feed direction, in which all tools featured compressive residual stresses.

The AlTiN coated tool featured the highest levels of tensile residual stresses in the cutting direction and austenite in the feed direction, in addition to a low level of compressive residual stress in ferrite in the feed direction. Therefore, the AlTiN coated tool had the worst stress state among the analysed tools, which is more

likely to result in further failure. Both multilayer and AlCrN coated tools had similar values of tensile residual stress in the ferrite phase in the cutting direction, as well as in the austenite phase and feed direction. However, the multilayer coated tool has significantly less tensile stress in the austenite phase in the cutting direction, as well as more compressive stress in the ferritic phase and feed direction, which results in an overall better stress state than AlCrN.

The residual stresses sources in metal cutting operations were already described by several authors [26], [44], [45]. The compressive residual stresses are generated by the plastic deformation of the machined layer that tends to primarily promote tensile stresses due to a greater amount of deformation on the surface than on the sub-surface. However, due to force equilibrium and geometric compatibility between the machined surface and sub-surface, compressive residual stresses will be formed in order to maintain the static equilibrium prior to the plastic deformation. This mechanism is illustrated in Figure 24, where the aforementioned effect is shown on a surface in static equilibrium.

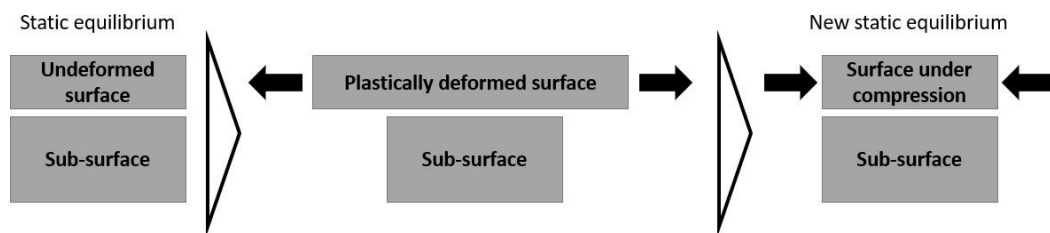


Figure 24: Compressive residual stress mechanism diagram.

In the previous diagram the surface and sub-surface are used to explain what happens with the grains during the process. Therefore, during the machining the material grains go through plastic deformation. Since the plastic deformation and temperature are more intense in the cutting direction, it is in this direction that residual stresses and grain deformation are also more intense.

The tensile residual stresses are a result of differences in thermal expansion and contraction of the superficial layer and sub-layer. When the workpiece absorbs the heat that comes from the primary shear zone, it goes through a thermal expansion process. However, the amount of heat in the surface layer is greater than in the subsurface. Therefore, the thermal expansion effect is stronger on the surface. To keep the geometric compatibility between the surface and the subsurface, which is still under the influence of heat, the surface layer will produce compressive stresses (similar to the compressive residual stress mechanism). After this rapid heating, the workpiece quickly cools down. At this point, the surface and subsurface are under opposite reactions of the same layers during heating. The rapid cooling will result in the shrinkage of the superficial layer and resultant tensile stress will be produced to maintain the geometric compatibility and force equilibrium. The tensile residual stress mechanism is illustrated in Figure 25, along with the heating and cooling effect on the material layers.

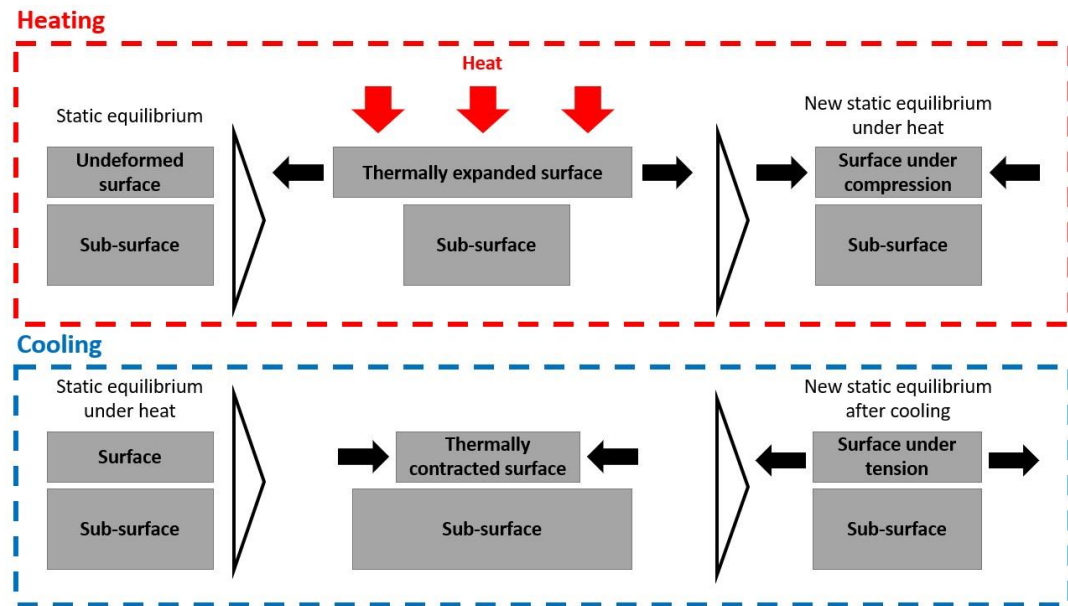


Figure 25: Tensile residual stress mechanism diagram.

The concept of layer, sub-layer, surface and sub-surface was used to illustrate the behaviour of the material grains under the mentioned conditions, which responds in a similar way when exposed to a quenching process. With this concept in mind, it is possible to explain the higher levels of residual stress in the austenitic phase compared to ferrite. This condition is related to the higher thermal expansion coefficient of austenite, shown in Table 3. Residual stresses act independently of external forces, whose source is given by the internal forces of the system (surface + sub-surface) in equilibrium state [46].

The tensile residual stresses measured on the machined workpiece reveal that the thermal effects during machining were more significant than any plastic deformation. Since the cutting zone is the source of heat during the cutting process, the thermal effect is more intense in the cutting direction than in the feed direction.

This behaviour is evidenced in tensile residual stresses in both phases and the cutting direction. The combination of tensile stresses in austenite with compressive stresses in ferrite shows the weaker thermal effect in the feed direction, as well as the stronger temperature effect in the austenite than in ferrite, given by the thermal expansion coefficient.

The performance of the coated tools during machining demonstrates the strong tensile effect produced by the AlTiN coated tool. The aluminium oxide-based tribofilms generated in the tool have low thermal conductivity. They act as a thermal barrier preventing heat penetration into the tool. Consequently, the heat generated in the PSDZ is distributed between the workpiece and the chip. Therefore, temperature tends to increase in the PSDZ, which promotes tensile residual stresses. A diagram in Figure 26 can illustrate the effect of the thermal barrier layer on the performance of the cutting tools.

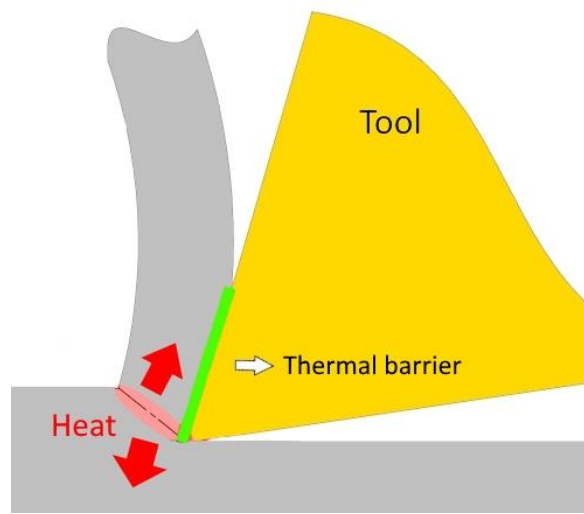


Figure 26: Thermal barrier effect schematics.

However, AlCrN and AlCrN/TiSiN coatings do not have the same performance as the AlTiN coating mainly due to the lower Al content in their chemical composition (67% in AlTiN compared to 50% in AlCrN). Literature states that AlCrN coatings with Al content between 70 and 75% can feature better tribological properties and oxidation resistance than AlTiN coatings if the FCC structure is predominant [47].

The presence of TiSiN in the multilayer tool is the reason for its better performance when compared to monolayer AlCrN. The XPS analysis of multilayer tool shows the complete oxidation of Si present on the coating in silicon oxides  $\text{SiO}_x$  at binding energy of 153 eV in the Si2s peak, where the film thickness is around 7 nm. The spectra as well as the sampling location are displayed in Figure 27.

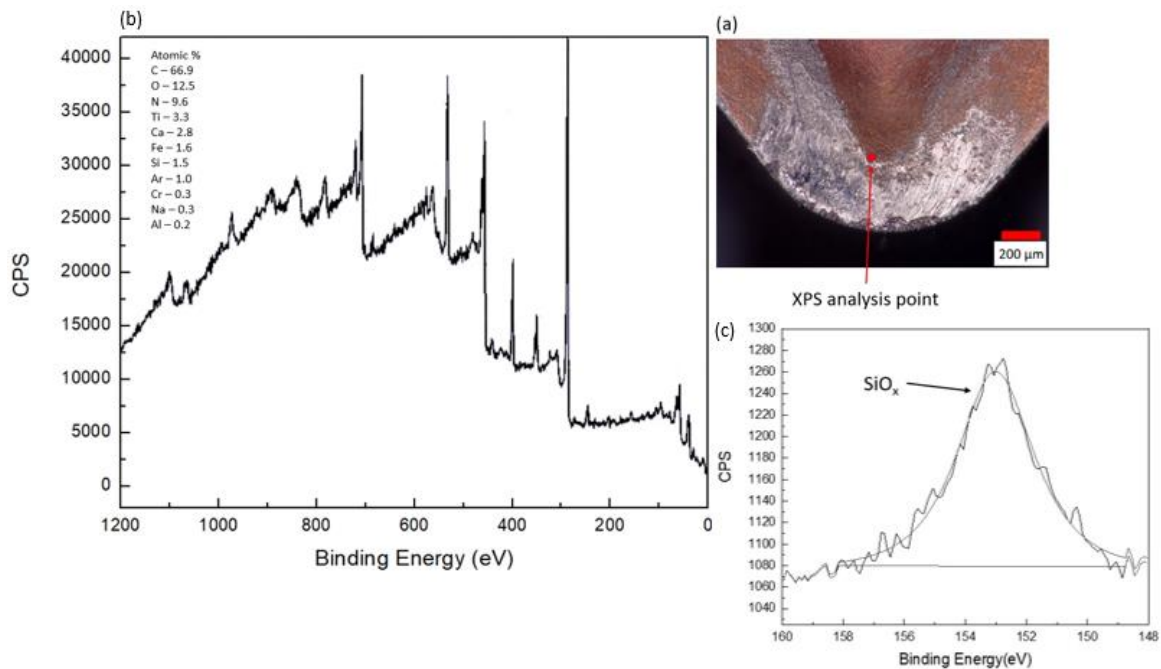


Figure 27: AlCrN/TiSiN coated tool XPS analysis (a) point selected for the analysis on the tool's rake face (b) full XPS spectra and (c) high resolution Si2s peak XPS spectra.

Besides also being a ceramic, the literature states that silicon oxides present a non-protective lubricious behaviour with low friction coefficient, which explains the lower cutting forces of multilayer coated tool when compared to AlCrN [27], [48]. Common Ti oxidation results in nonstoichiometric oxides as well as  $TiO_2$ , where both on them are not protective [28]. The non-complex Cr oxides are also non-protective phases with lubricious properties [49]. The lack of protection results in higher heat diffusion into the tool. As result, the tool wear is accelerated and the heat amount diffused into the workpiece is diminished.

### 4.3 – CORROSION TESTS

The typical open circuit potential (OCP) versus time for each type of machined surfaces pre-polarization measurements is presented in Figure 28.

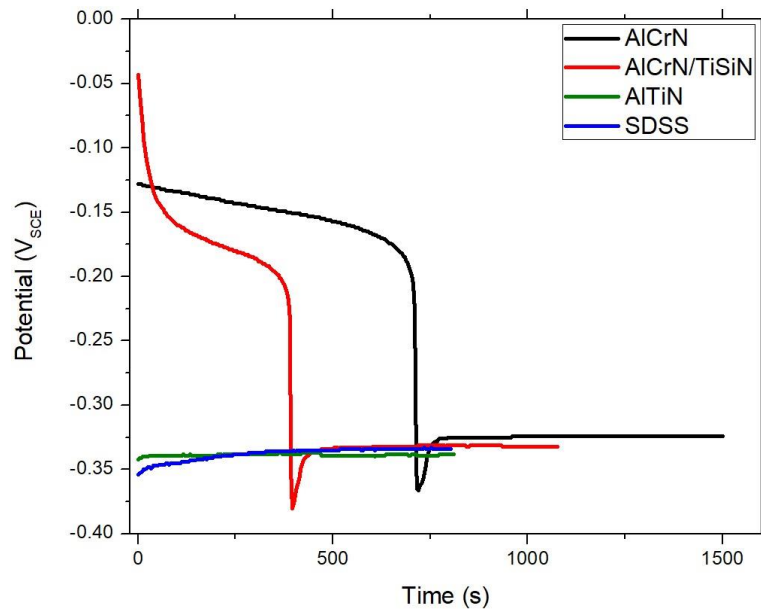


Figure 28: Typical open circuit potential versus time for of AICrN, AICrN/TiSiN, AITiN and SDSS samples.

The graph above shows that overall SDSS and AITiN samples had similar response to solution exposure while AICrN and AICrN/TiSiN presented unique response, based on the time necessary to reach a stable potential. The differences in the sample potential before stabilization are related with the material tendency to corrosion. More positive potentials than OCP shows instability and tendency to

corrosion while potentials more negative than OCP reveal a stable sample (less tendency to corrosion). All analysed samples featured a similar stable open circuit potential. Following the OCP stage, the results obtained from the potentiodynamic anodic polarization are displayed in Figure 29.

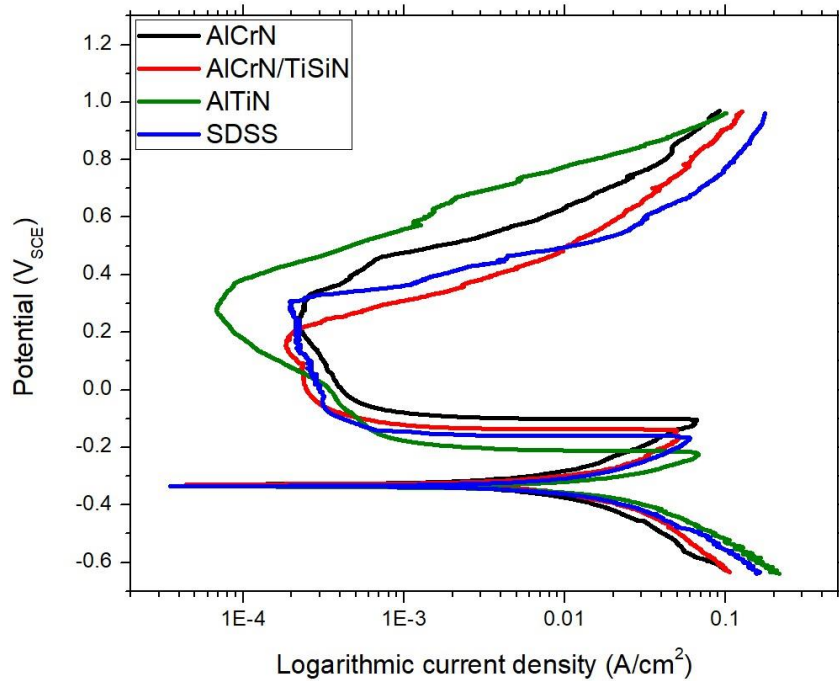


Figure 29: Typical polarization curves of AlCrN, AlCrN/TiSiN, AlTiN and SDSS samples.

These are typical polarization curves obtained in this study (the remaining curves can be found in the appendix), they show that all samples have a similar corrosion potential ( $E_{CORR}$ ) of around  $-0.3 V_{SCE}$ . For comparison purposes the Figure 30 shows the corrosion potential and current density for the analyzed surfaces.

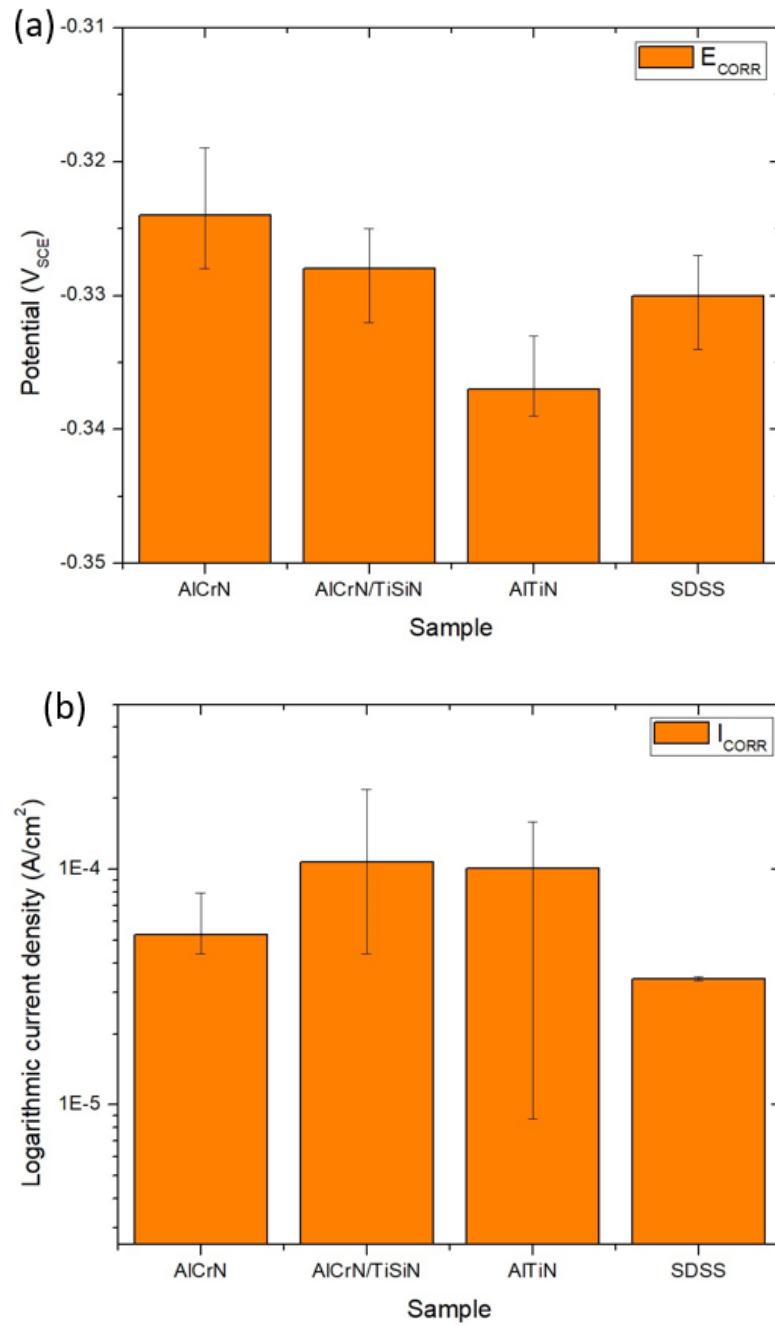


Figure 30: Corrosion potential (a) and current density (b) statistics.

Overall, the AlCrN, AlCrN/TiSiN and SDSS sample showed similar corrosion potential, while AlTiN sample corrosion potential is slightly more negative. The AlCrN and AlCrN/TiSiN machined samples had a similar corrosion current density ( $i_{CORR}$ ) ( $5 \times 10^{-5} \text{ A/cm}^2$  and  $1 \times 10^{-4} \text{ A/cm}^2$  respectively) and slightly higher than the SDSS sample ( $3 \times 10^{-5} \text{ A/cm}^2$ ). The AlTiN machined sample however, presented a higher variation in its corrosion current density being in a range from  $1 \times 10^{-5}$  to  $3 \times 10^{-4} \text{ A/cm}^2$ . The Figure 31 shows the potential and current data for the passivation stage during polarization measurements.

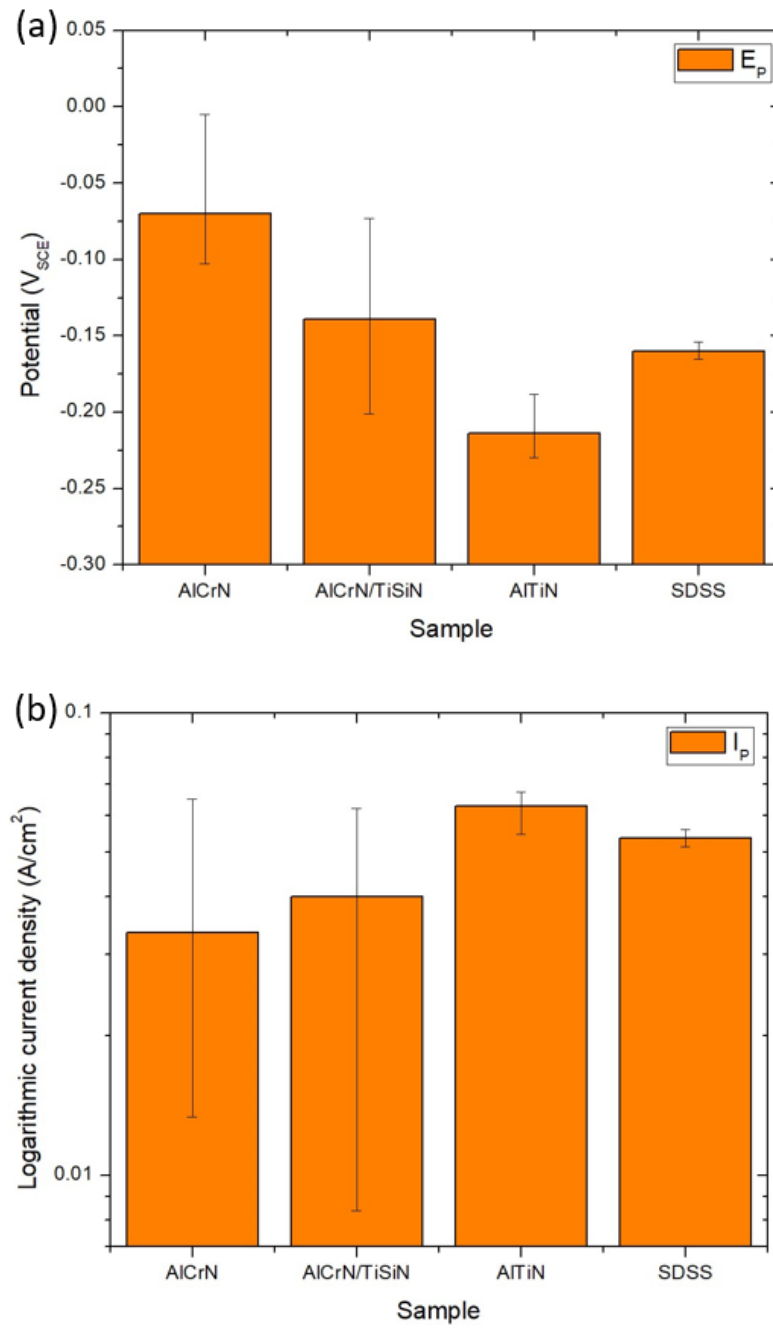


Figure 31: Passivation potential (a) and current density (b) statistics.

The samples had different passivation potentials ( $E_P$ ) during the active phase. AlTiN has the lowest passivation potential around  $-0.23 V_{SCE}$ , followed by the benchmark with values around  $-0.17 V_{SCE}$ . Passivation developed later in the AlCrN than in the previous two samples, with potential around  $-0.08 V_{SCE}$ , being the highest average passivation potential. The AlCrN/TiSiN surface shows a high variation in its passivation potential, with values between  $-0.2$  and  $-0.08 V_{SCE}$ . Apart from differences in the potential, all samples had similar passivation current density ( $i_P$ ) of between  $3 \times 10^{-3}$  and  $6 \times 10^{-3} A/cm^2$ . However, the variation of AlTiN and SDSS samples are small compared to the AlCrN and AlCrN/TiSiN samples.

Passive behaviour was observed in the samples following passivation. The potential ( $E_{PASSIVE}$ ) and current density ( $i_{PASSIVE}$ ) were analyzed at the beginning of this stage, where the average values are shown in Figure 32.

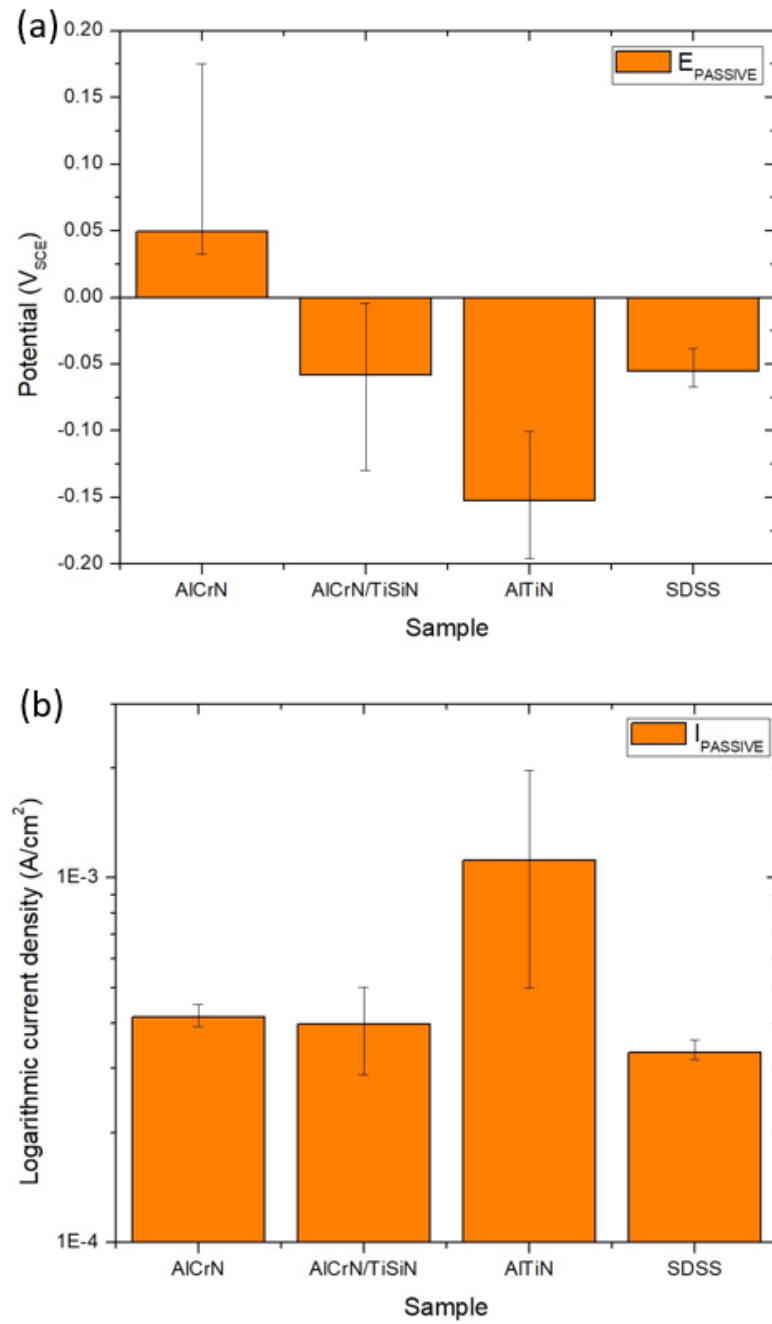


Figure 32: Passive stage potential (a) and current density (b) statistics.

The AlTiN sample typically presented a smooth transition to the passive region, starting around  $1 \times 10^{-3}$  A/cm<sup>2</sup> and -0.15 V<sub>SCE</sub>, while the passive stage of the benchmark and AlCrN/TiSiN samples began close to each other and slightly later than AlTiN, around  $3 \times 10^{-4}$  A/cm<sup>2</sup> and -0.05 V<sub>SCE</sub>. The AlCrN sample had the more positive average passive potential around 0.05 V<sub>SCE</sub> however, the passive stage started near the same current density as AlCrN/TiSiN and SDSS. Polarization measurements data shows the same sample trend for both passivation and passive stage. While the passive stage of AlCrN, AlCrN/TiSiN and SDSS samples did not show a huge variation of current density, the AlTiN sample showed an almost constant current decay until reached its minimum values before the starting point of trans passive stage. After a certain potential the current density started to increase once more, which indicates a transpassive stage. The transpassivation is related to the passive film break-down, resulting in increase in the current density and pitting corrosion formation. The transpassive potential ( $E_T$ ) and current density ( $i_T$ ) of the analyzed samples are shown in Figure 33.

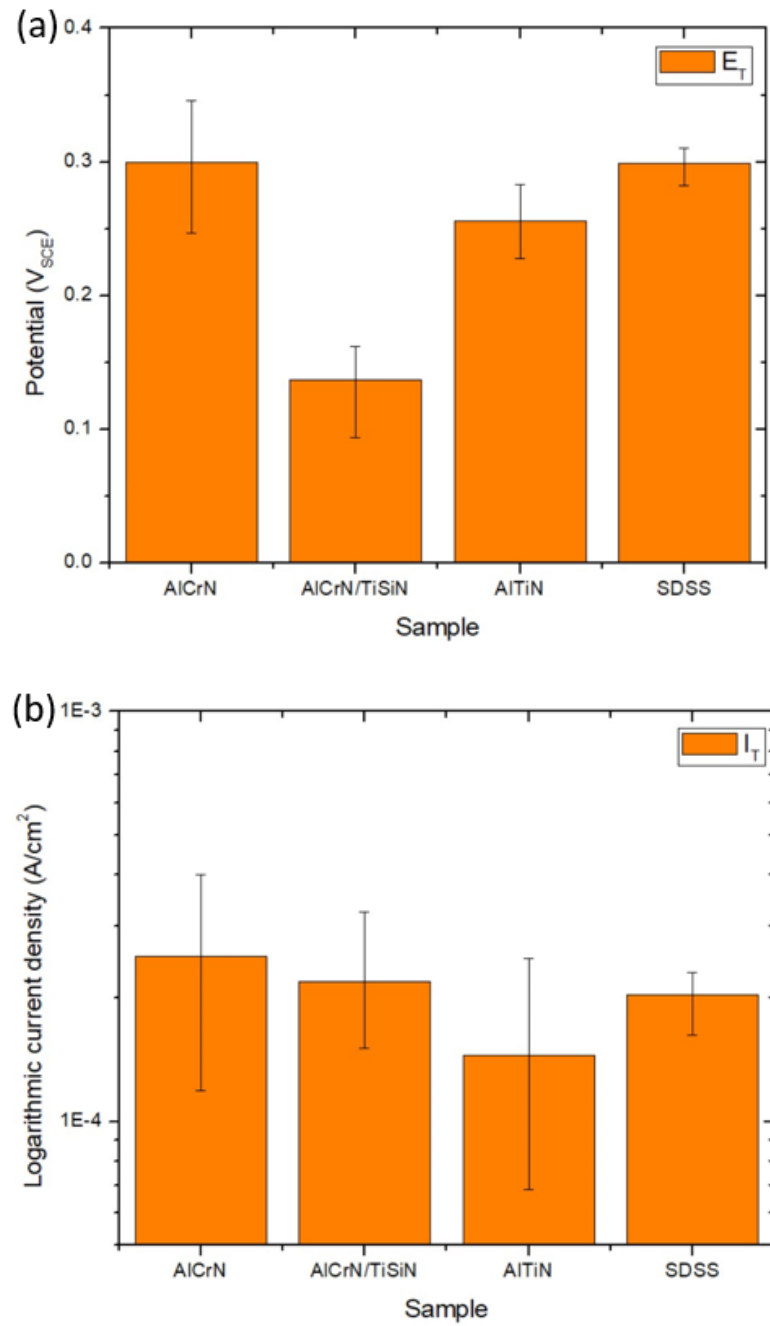


Figure 33: Transpassive potential (a) and current density (b) statistics.

On average, the AlCrN, AlTiN and SDSS samples had similar transpassivation potential, which is in between 0.25 and 0.3  $V_{SCE}$ . However, the AlCrN/TiSiN sample showed an early transpassivation at potential around 0.12  $V_{SCE}$ . In terms of current density all the samples started the transpassive stage around the same point on average. The results achieved show that on average the AlTiN sample presents an earlier passivation and passive stage than other samples but a similar corrosion and transpassivation potential. This results in a longer passive stage, being beneficial for the sample. The SDSS sample had the second longest passive stage and presented the lower variation in terms of potential and current density. The AlCrN/TiSiN sample had similar behaviour to SDSS however, it also showed higher variation of potential and current. The AlCrN sample presented later passivation and short passive stage compared to the other samples, which reflects in a surface with less corrosion protection.

According to literature, the alloying elements, specially Cr, are the main responsible for the formation of resistant passive films [30]. Therefore, the Cr content of each machined sample was analyzed and is shown in Figure 34. The only differences in Cr content were observed near the surface, thus the data displayed in Figure 34 corresponds to an EDS reading at 0.17 minutes of sputtering (time was used for better sputtering control).

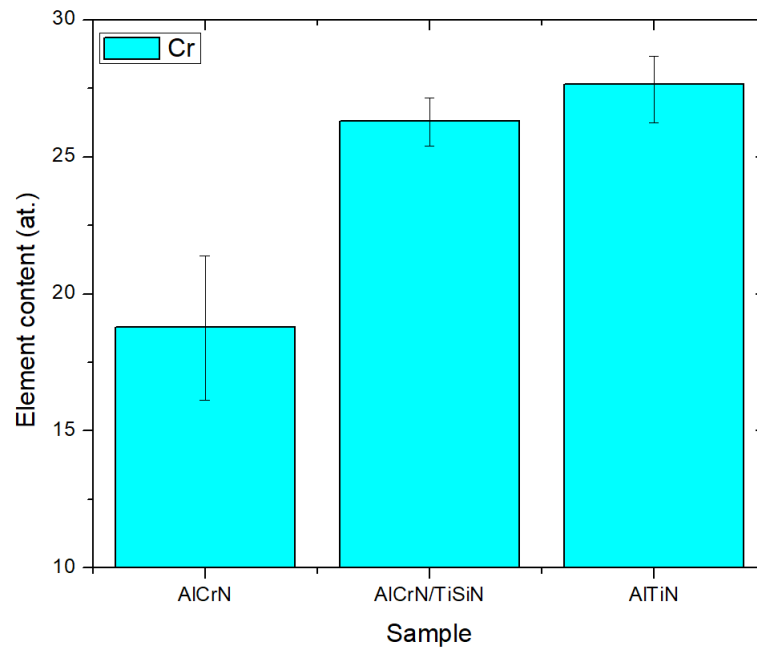


Figure 34: Atomic Cr content on the machined samples surface.

The Cr content of AlCrN is lower than AlCrN/TiSiN and AlTiN, which results in its typical later passivation. However, the Cr content of AlCrN/TiSiN and AlTiN are quite similar, which is not enough to promote the differences displayed in the polarization measurement curves. SDSS sample was not analyzed since it is the benchmark curve.

A current study show relation between surface roughness and corrosion susceptibility of materials, where a better surface finishing increases passivation tendency [50]. In the present study, the benchmark with a smoother surface had lower values of  $i_{CORR}$  than the machined samples at the same  $E_{CORR}$ . Similar to the AlTiN coating, it featured a longer passive region than the AlCrN and AlCrN/TiSiN coatings. An exception was noted during the active phase prior to passivation,

where the benchmark had a higher activation slope than the AlTiN coating. In addition to surface finish, plastic deformation also influences the corrosion behaviour of materials. Studies show that corrosion susceptibility can either improve or deteriorate, depending on the amount of surface plastic deformation [51]–[53]. Therefore, the corrosion susceptibility of the material is influenced not only by surface finish, but also by the plastic deformation. This can explain why the benchmark sample featured a slightly higher passivation potential than the AlTiN coatings. As mentioned in [51], lower levels of plastic deformation impede corrosion formation in the material. The plastic deformation observed in AlTiN sample was milder compared to other machined samples, which can be related to its lowest corrosion susceptibility.

According to the polarization curves the best electrochemical condition is during the passive stage due to the presence of passive films that lowers the corrosion rate. The initial and end portions of passive stage are not recommended to stay due to instabilities in the passive film. Ideally the sample would stay in the middle of passive region on the polarization curves, where the passivation would start early and the transpassivation would happen in a high potential (noble potential).

The stress cracking corrosion study investigated the influence of the residual stresses after machining along with crack initiation and propagation. Figure 35 shows the crack density results, which is given by the division of the total

crack length by the sample area. The displayed results are separated in the feed and cutting directions.

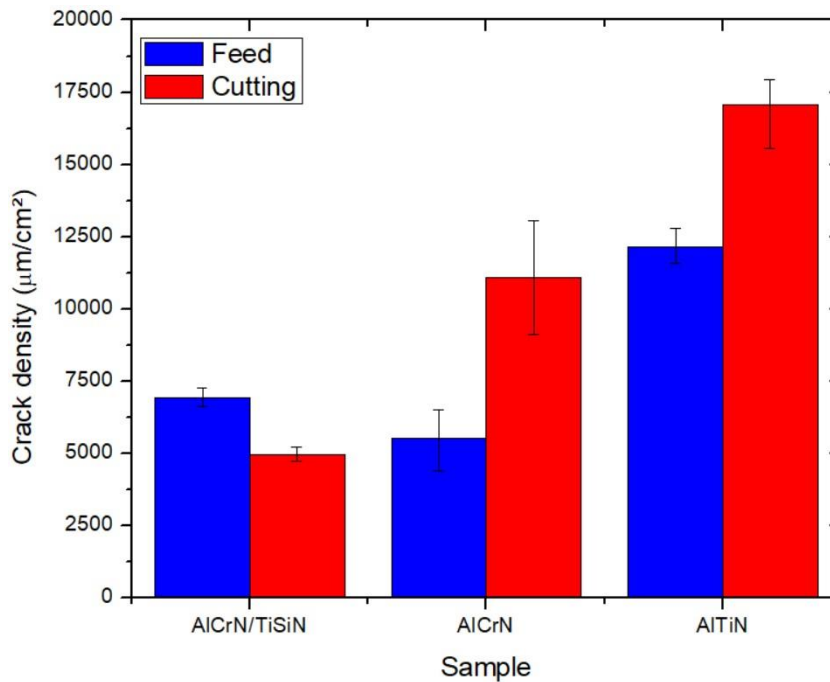


Figure 35: Crack density after the SCC test.

After the SCC test, no cracks were observed in the benchmark samples. The crack density of the machined samples follows the same distribution as that of the residual stresses in the austenitic phase, which featured the highest stress levels out of the two analysed phases. Scanning microscopy images of the cracked surfaces are displayed in Figure 36.

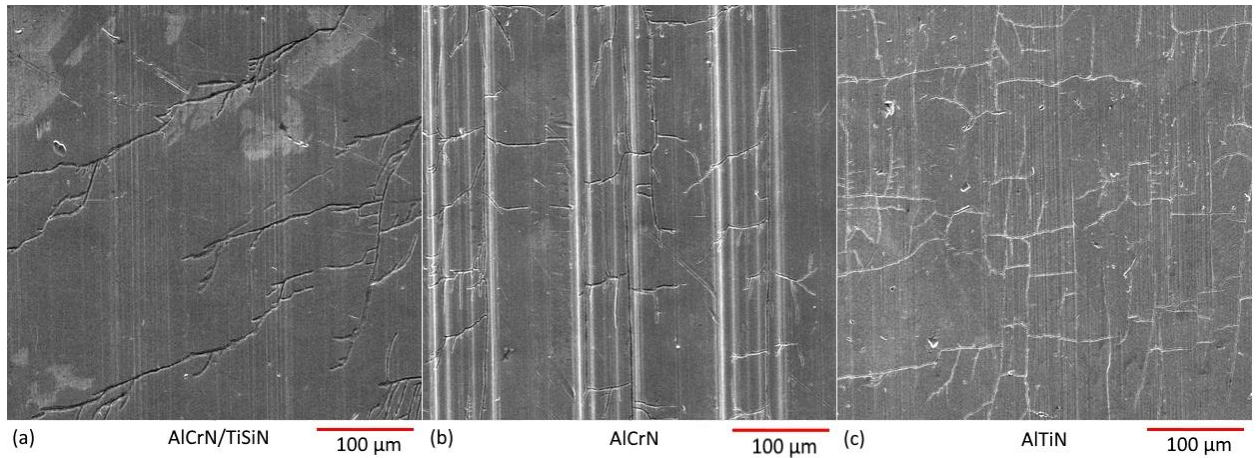


Figure 36: Cracked surfaces.

These SEM images present the average behaviour of the samples after the SCC test. The difference between the amounts of cracks between the analysed samples is visible. The AlTiN coated tool has a higher number of cracks than the AlCrN and multilayer ones. The optical cross-section images were prepared to analyse the crack nucleation sites displayed in Figure 37. The images show the cracks orthogonal to the cutting direction (cutting), as well as the feed direction (feed).

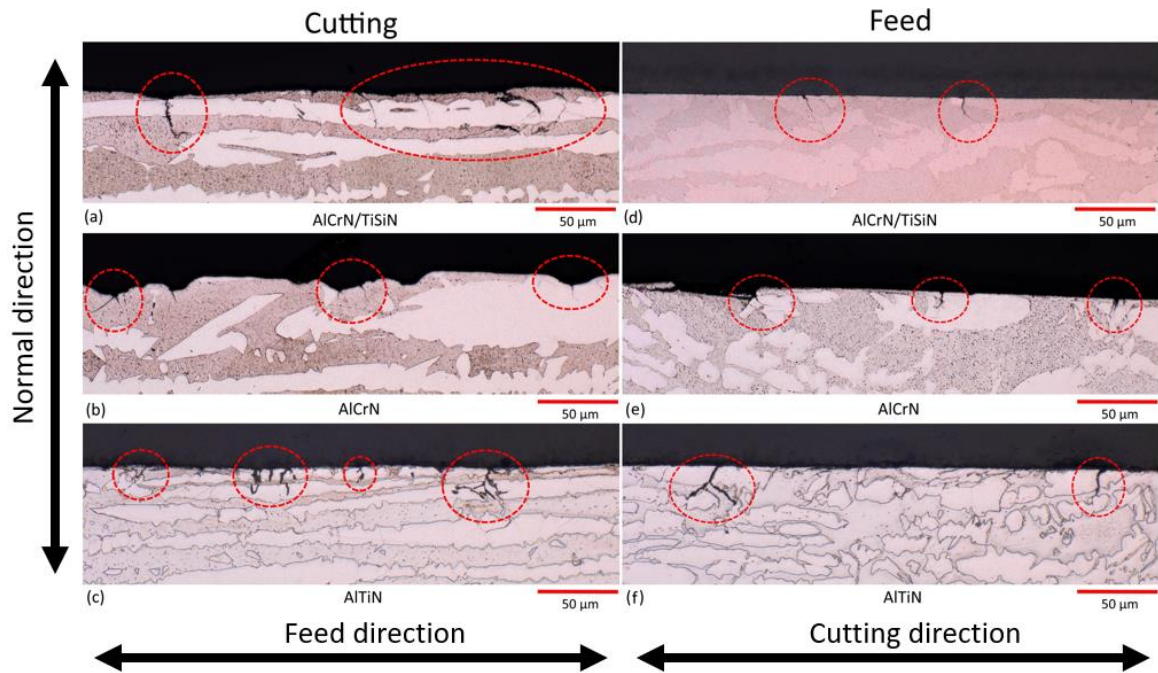


Figure 37: Cracks cross-section optical analysis. AlCrN/TiSiN coated tool cutting (a) and (d) feed direction, AlCrN coated tool cutting (b) and (e) feed, AlTiN coated tool cutting (c) and (f) feed.

Residual stress analysis shows that cracks were initiated in both phases in the cutting direction. In the feed direction, the cracks were mostly concentrated in the austenitic phase. The images show that the cracks propagate through the grains into the material. Wider cracks are observed in the AlTiN coated tool machined cross-section, as a result of its higher residual stresses and crack density. Undersurface damage is visible on the machined cross-section using a multilayer coated tool in the cutting direction, possibly due to the random propagation of adjacent cracks.

## CHAPTER 5 – CONCLUSIONS

The adopted experimental method, as well as the results achieved on the corrosion behaviour study of machined super duplex stainless steel using cutting tool with three different PVD coatings, can lead to the following conclusions:

- **Machining performance:** The tool life results show that the life of the AlTiN coated tool is two times longer than AlCrN and AlCrN/TiSiN. This result is supported not only by SEM figures, but also by the XRD results, which shows formation of aluminium oxide tribo-films. The presence of aluminum oxide during the cutting process is beneficial for the tool, promoting resistance against adhesion and heat diffusion into the tool [41].
- **Surface integrity:** The AlTiN coated tool produced not only the smoothest surface among all tools at the same cutting conditions, but also the least work-hardened surface. This property can be related to the forces generated during the cutting process. These two aspects are associated with the previously mentioned tribological conditions during machining. However, the residual stress measurements reveal higher levels of tensile residual stress in the AlTiN coated tool, due to the thermal-barrier effect of the coating, which redirects the heat generated during the process to the workpiece and chips. This behaviour was less pronounced for multilayer tool due to the lubricious silicon oxides formation, while AlCrN coated tool behaved in between.

- Corrosion behaviour: The results show that the surface machined by an AlTiN coated tool has corrosion resistance compared to the other samples. Similar to the polished benchmark sample, early passivation and a wider passive region improves the ability of the AlTiN coated tool to protect the surface from corrosion.
- Stress cracking corrosion: In contrast to the polarization results, the AlTiN coated tool surface featured a high number of cracks. Residual stress measurements reveal that the multilayer coated tool had the smallest crack density. Additionally, the residual stress differences in ferrite and austenite in the feed direction only yielded crack initiation in the ferrite.

Apart from featuring improved machining performance and surface finish compared to other PVD coated tools, the AlTiN coated tool had the highest tensile residual stress, which had the most detrimental impact on crack initiation in SDSS surfaces. In contrast with AlTiN, the crack density was less intense in the AlCrN/TiSiN sample, due to lower tensile residual stresses.

In almost all applications, component functionality is more important than production rate. For offshore pipeline components used in oil extraction, the component corrosion resistance must not be exchanged for longer cutting tool life due to the potentially catastrophic consequences of integrity loss.

## **CHAPTER 6 – SUGGESTION TO FUTURE WORKS**

Based on the current study, several topics are suggested for further experimental investigations:

- Evaluation of temperature distribution during the cutting process for the mentioned tools.
- Evaluation of post-machining surface treatment methods to reduce or eliminate the tensile residual stresses, as well as their corrosion behaviour.
- Investigation of the effects of surface roughness following machining and plastic deformation on the corrosion behaviour of SDSS.

## REFERENCES

- [1] B. D. Beake *et al.*, “Wear performance of different PVD coatings during hard wet end milling of H13 tool steel,” *Surf. Coatings Technol.*, vol. 279, pp. 118–125, Oct. 2015.
- [2] A. Ben Rhouma, C. Braham, M. E. Fitzpatrick, J. Leidion, and H. Sidhom, “Effects of Surface Preparation on Pitting Resistance, Residual Stress, and Stress Corrosion Cracking in Austenitic Stainless Steels,” *J. Mater. Eng. Perform.*, vol. 10, no. 5, pp. 507–514, Oct. 2001.
- [3] J. Rajaguru and N. Arunachalam, “Investigation on machining induced surface and subsurface modifications on the stress corrosion crack growth behaviour of super duplex stainless steel,” *Corros. Sci.*, vol. 141, no. July, pp. 230–242, Aug. 2018.
- [4] C. I. Ossai, “Advances in Asset Management Techniques: An Overview of Corrosion Mechanisms and Mitigation Strategies for Oil and Gas Pipelines,” *ISRN Corros.*, vol. 2012, pp. 1–10, 2012.
- [5] J.-O. Nilsson, “Super duplex stainless steels,” *Mater. Sci. Technol.*, vol. 8, no. 8, pp. 685–700, Aug. 1992.
- [6] J. M. Pardal, S. S. M. Tavares, M. C. Fonseca, J. A. de Souza, R. R. A. Côte, and H. F. G. de Abreu, “Influence of the grain size on deleterious phase precipitation in superduplex stainless steel UNS S32750,” *Mater. Charact.*, vol. 60, no. 3, pp. 165–172, Mar. 2009.

- [7] Z. Cvijović and G. Radenković, “Microstructure and pitting corrosion resistance of annealed duplex stainless steel,” *Corros. Sci.*, vol. 48, no. 12, pp. 3887–3906, Dec. 2006.
- [8] M. Pohl, O. Storz, and T. Glogowski, “Effect of intermetallic precipitations on the properties of duplex stainless steel,” *Mater. Charact.*, vol. 58, no. 1, pp. 65–71, Jan. 2007.
- [9] H. Tan, Y. Jiang, B. Deng, T. Sun, J. Xu, and J. Li, “Effect of annealing temperature on the pitting corrosion resistance of super duplex stainless steel UNS S32750,” *Mater. Charact.*, vol. 60, no. 9, pp. 1049–1054, Sep. 2009.
- [10] K. Fushimi, K. Yanagisawa, T. Nakanishi, Y. Hasegawa, T. Kawano, and M. Kimura, “Microelectrochemistry of dual-phase steel corroding in 0.1M sulfuric acid,” *Electrochim. Acta*, vol. 114, pp. 83–87, Dec. 2013.
- [11] J.-O. Nilsson, P. Kangas, A. Wilson, and T. Karlsson, “Mechanical properties, microstructural stability and kinetics of  $\sigma$ -phase formation in 29Cr-6Ni-2Mo-0.38N superduplex stainless steel,” *Metall. Mater. Trans. A*, vol. 31, no. 1, pp. 35–45, Jan. 2000.
- [12] C. Requirements, C. Requirements, S. Manual, and P. Count, “Standard Specification for Resistant , Duplex ( Austenitic / Ferritic ) for General,” 2018.
- [13] S. S. M. Tavares, V. G. Silva, J. M. Pardal, and J. S. Corte, “Investigation of stress corrosion cracks in a UNS S32750 superduplex stainless steel,” *Eng. Fail. Anal.*, vol. 35, pp. 88–94, Dec. 2013.

- [14] I. Alvarez-Armas and S. Degallaix-Moreuil, *Duplex Stainless Steels*, 1st ed. Hoboken, NJ, USA: John Wiley & Sons, Inc., 2013.
- [15] A. J. Leonard, A. Gregori, and P. Woolin, "Point counting of intermetallic phase precipitates in ferritic-austenitic stainless steels," *Weld. World*, vol. 51, no. 11–12, pp. 20–28, Nov. 2007.
- [16] H. K. D. H. Bhadeshia and R. Honeycomb, *Steels: Microstructure and Properties*, 3rd editio. Oxford - UK: Elsevier, 2006.
- [17] R. N. Gunn, *Duplex stainless steels*, 1st editio. Woodhead Publishing Limited, 1997.
- [18] J. R. Davis, *Stainless Steel - ASM Speciality Handbook*, 2nd ed. USA: ASM International, 2000.
- [19] Z. Zhang, H. Jing, L. Xu, Y. Han, L. Zhao, and J. Zhang, "Influence of microstructure and elemental partitioning on pitting corrosion resistance of duplex stainless steel welding joints," *Appl. Surf. Sci.*, vol. 394, pp. 297–314, Feb. 2017.
- [20] P. Paulraj and R. Garg, "EFFECT OF INTERMETALLIC PHASES ON CORROSION BEHAVIOR AND MECHANICAL PROPERTIES OF DUPLEX STAINLESS STEEL AND SUPER-DUPLEX STAINLESS STEEL," *Adv. Sci. Technol. Res. J.*, vol. 9, no. 27, pp. 87–105, 2015.
- [21] E. Angelini, B. De Benedetti, and F. Rosalbino, "Microstructural evolution and localized corrosion resistance of an aged superduplex stainless steel," *Corros. Sci.*, vol. 46, no. 6, pp. 1351–1367, Jun. 2004.

- [22] S. S. M. Tavares, J. M. Pardal, L. D. Lima, I. N. Bastos, A. M. Nascimento, and J. A. de Souza, “Characterization of microstructure, chemical composition, corrosion resistance and toughness of a multipass weld joint of superduplex stainless steel UNS S32750,” *Mater. Charact.*, vol. 58, no. 7, pp. 610–616, Jul. 2007.
- [23] S. Topolska and J. Labanowski, “Effect of microstructure on impact toughness of duplex and superduplex stainless steels,” *J. Achiev. Mater. Manuf. Eng.*, vol. 36, no. 2, pp. 142–149, 2009.
- [24] E. M. Trent and P. K. Wright, *Metal Cutting*, 4th Editio. Butterworth-Heinemann, 2000.
- [25] M. C. Shaw, *Metal Cutting Pinciples*, Second Edi. 2004.
- [26] D. A. Stephenson and J. S. Agapiou, *Metal Cutting Theory and Practice*, Thrid Edit. Boca Raton, FL: CRC Press, 2016.
- [27] J. M. F. Paiva, F. L. Amorim, P. C. Soares, S. C. Veldhuis, L. A. Mendes, and R. D. Torres, “Tribological behavior of superduplex stainless steel against PVD hard coatings on cemented carbide,” *Int. J. Adv. Manuf. Technol.*, vol. 90, no. 5–8, pp. 1649–1658, May 2017.
- [28] J. M. F. de Paiva *et al.*, “Frictional and wear performance of hard coatings during machining of superduplex stainless steel,” *Int. J. Adv. Manuf. Technol.*, vol. 92, no. 1, pp. 423–432, Sep. 2017.
- [29] J. P. Davim, *Surface integrity in machining*. London: Springer London, 2010.
- [30] D. A. Jones, *Principles and Prevention of Corrosion*, 2nd Editio. Upper

Saddle River, NJ: Prentice Hall, 1996.

- [31] J. Cui, I. Park, C. Kang, and K. Miyahara, "Degradation of Impact Toughness due to Formation of R Phase in High Nitrogen 25Cr-7Ni-Mo Duplex Stainless Steels," *ISIJ Int.*, vol. 41, no. 2, pp. 192–195, 2001.
- [32] I. N. Bastos, S. S. M. Tavares, F. Dalard, and R. P. Nogueira, "Effect of microstructure on corrosion behavior of superduplex stainless steel at critical environment conditions," *Scr. Mater.*, vol. 57, no. 10, pp. 913–916, 2007.
- [33] J. Nowacki and A. Łukojc, "Microstructural transformations of heat affected zones in duplex steel welded joints," *Mater. Charact.*, vol. 56, no. 4-5 SPEC. ISS., pp. 436–441, 2006.
- [34] J. Smiderle, J. M. Pardal, S. S. M. Tavares, and A. C. N. Vidal, "Premature failure of superduplex stainless steel pipe by pitting in sea water environment," *Eng. Fail. Anal.*, vol. 46, pp. 134–139, 2014.
- [35] G. Królczyk, M. Gajek, and S. Legutko, "Effect of the cutting parameters impact on tool life in duplex stainless steel turning process," *Teh. Vjesn.*, vol. 20, no. 4, pp. 587–592, 2013.
- [36] E. C. Bordinassi, G. F. Batalha, S. Delijaicov, N. B. De Lima, S. Paulo, and F. D. E. Industrial, "Superficial integrity analysis in a super duplex stainless steel after turning," *J. Achiev. Mater. Manuf. Eng.*, vol. 18, no. 1, pp. 335–338, 2006.
- [37] C. A. De Oliveira Junior, A. E. Diniz, and R. Bertazzoli, "Correlating tool wear, surface roughness and corrosion resistance in the turning process of super

- duplex stainless steel,” *J. Brazilian Soc. Mech. Sci. Eng.*, vol. 36, no. 4, pp. 775–785, 2014.
- [38] J. L. Endrino, G. S. Fox-Rabinovich, and C. Gey, “Hard AlTiN, AlCrN PVD coatings for machining of austenitic stainless steel,” *Surf. Coatings Technol.*, vol. 200, no. 24, pp. 6840–6845, Aug. 2006.
- [39] J. Nomani, A. Pramanik, T. Hilditch, and G. Littlefair, “Machinability study of first generation duplex (2205), second generation duplex (2507) and austenite stainless steel during drilling process,” *Wear*, vol. 304, no. 1–2, pp. 20–28, Jul. 2013.
- [40] G. S. Fox-rabinovich and G. E. Totten, *Self-Organization During Friction*, 1st ed. Boca Raton, FL: CRC Press, 2006.
- [41] J. M. F. de Paiva *et al.*, “Frictional and wear performance of hard coatings during machining of superduplex stainless steel,” *Int. J. Adv. Manuf. Technol.*, vol. 92, no. 1–4, pp. 423–432, Sep. 2017.
- [42] L. Filice, F. Micari, S. Rizzuti, and D. Umbrello, “A critical analysis on the friction modelling in orthogonal machining,” *Int. J. Mach. Tools Manuf.*, vol. 47, no. 3–4, pp. 709–714, Mar. 2007.
- [43] W. Chen, “Cutting forces and surface finish when machining medium hardness steel using CBN tools,” vol. 40, pp. 455–466, 2000.
- [44] A. Devillez, G. Le Coz, S. Dominiak, and D. Dudzinski, “Dry machining of Inconel 718, workpiece surface integrity,” *J. Mater. Process. Technol.*, vol. 211, no. 10, pp. 1590–1598, Oct. 2011.

- [45] F. Gunnberg, M. Escursell, and M. Jacobson, “The influence of cutting parameters on residual stresses and surface topography during hard turning of 18MnCr5 case carburised steel,” *J. Mater. Process. Technol.*, vol. 174, no. 1–3, pp. 82–90, May 2006.
- [46] E. Brinksmeier, J. T. Cammett, W. König, P. Leskovar, J. Peters, and H. K. Tönshoff, “Residual Stresses - Measurement and Causes in Machining Processes,” *CIRP Ann. - Manuf. Technol.*, vol. 31, no. 2, pp. 491–510, 1982.
- [47] J. L. Endrino *et al.*, “Oxidation tuning in AlCrN coatings,” *Surf. Coatings Technol.*, vol. 201, no. 8, pp. 4505–4511, Jan. 2007.
- [48] C. T. Guo, D. Lee, and P. C. Chen, “Deposition of TiSiN coatings by arc ion plating process,” *Appl. Surf. Sci.*, vol. 254, no. 10, pp. 3130–3136, Mar. 2008.
- [49] J. Yuan *et al.*, “Tribo-films control in adaptive TiAlCrSiYN/TiAlCrN multilayer PVD coating by accelerating the initial machining conditions,” *Surf. Coatings Technol.*, vol. 294, pp. 54–61, May 2016.
- [50] R. Walter and M. B. Kannan, “Influence of surface roughness on the corrosion behaviour of magnesium alloy,” *Mater. Des.*, vol. 32, no. 4, pp. 2350–2354, Apr. 2011.
- [51] U. Kamachi Mudali, P. Shankar, S. Ningshen, R. K. Dayal, H. S. Khatak, and B. Raj, “On the pitting corrosion resistance of nitrogen alloyed cold worked austenitic stainless steels,” *Corros. Sci.*, vol. 44, no. 10, pp. 2183–2198, Oct. 2002.
- [52] H. Luo, H. Su, G. Ying, C. Dong, and X. Li, “Effect of cold deformation on the

electrochemical behaviour of 304L stainless steel in contaminated sulfuric acid environment,” *Appl. Surf. Sci.*, vol. 425, pp. 628–638, Dec. 2017.

- [53] V. Azar, B. Hashemi, and M. Rezaee Yazdi, “The effect of shot peening on fatigue and corrosion behavior of 316L stainless steel in Ringer’s solution,” *Surf. Coatings Technol.*, vol. 204, no. 21–22, pp. 3546–3551, Aug. 2010.

## APPENDIX

This appendix shows all the OCP and polarization curves obtained in this work.

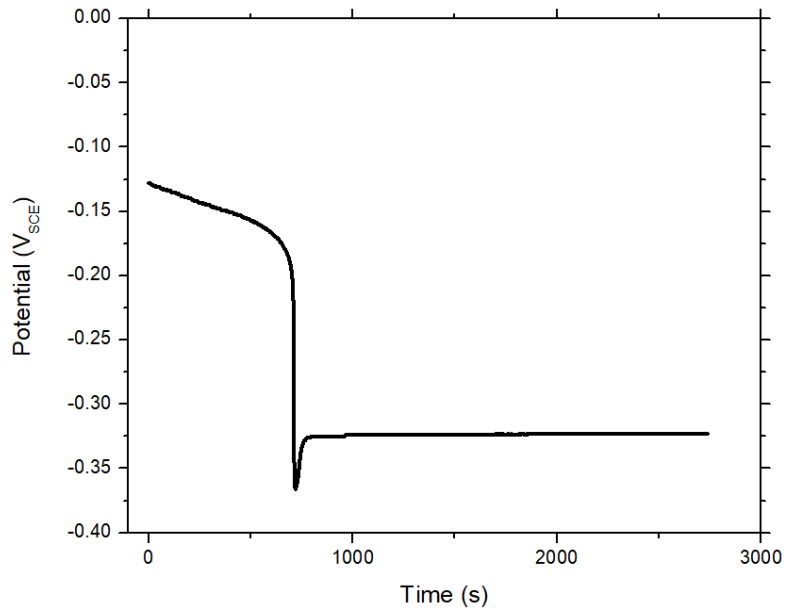


Figure A1: OCP curve AICrN sample 1.

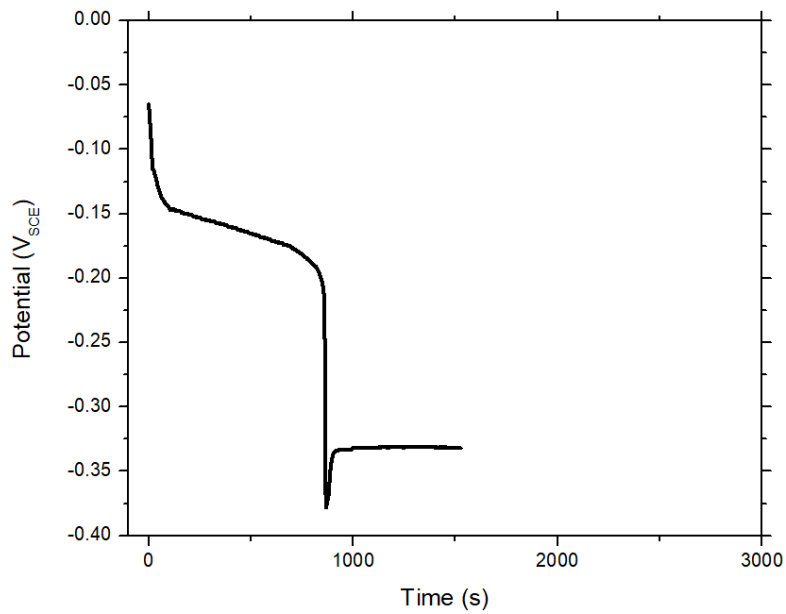


Figure A2: OCP curve AICrN sample 2.

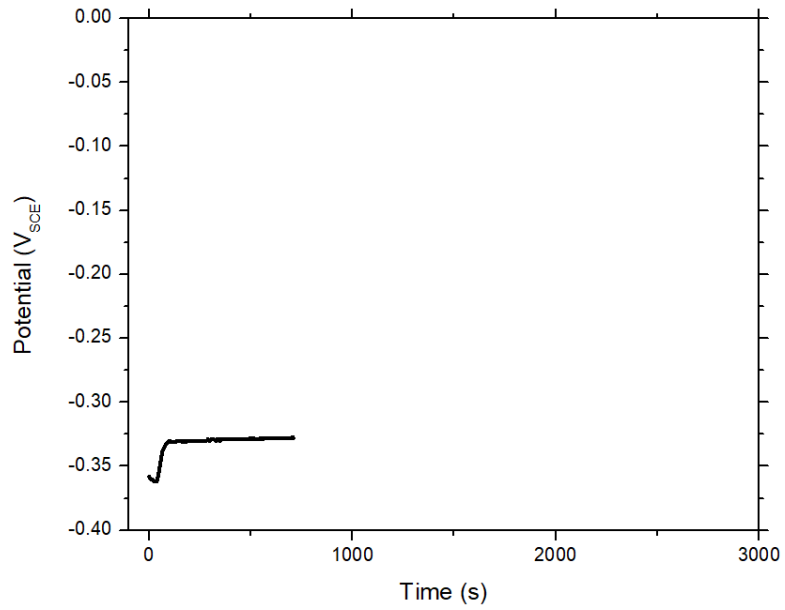


Figure A3: OCP curve AlCrN sample 3.

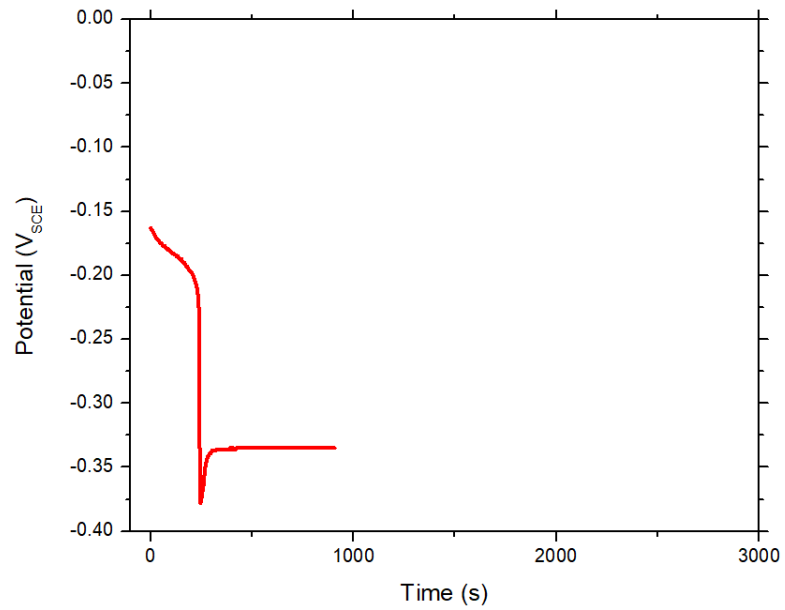


Figure A4: OCP curve AlCrN/TiSiN sample 1.

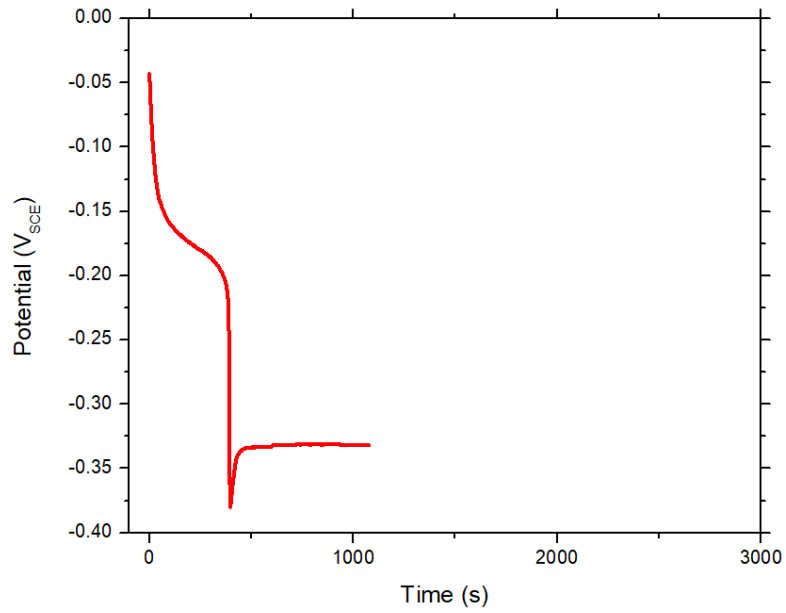


Figure A5: OCP curve AICrN/TiSiN sample 2.

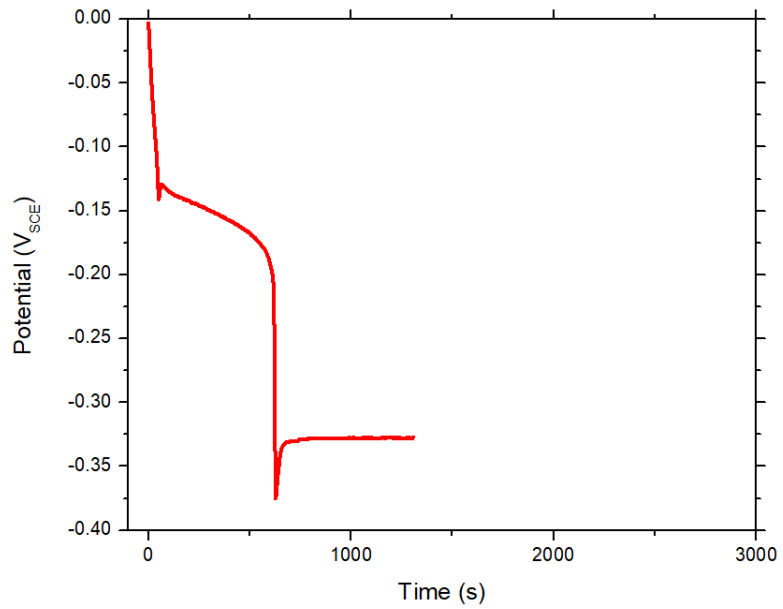


Figure A6: OCP curve AICrN/TiSiN sample 3.

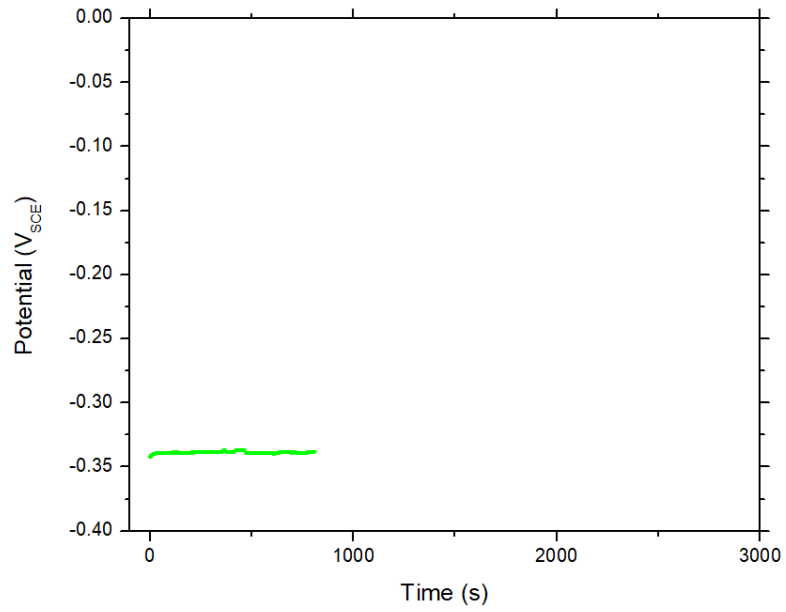


Figure A7: OCP curve AlTiN sample 1.

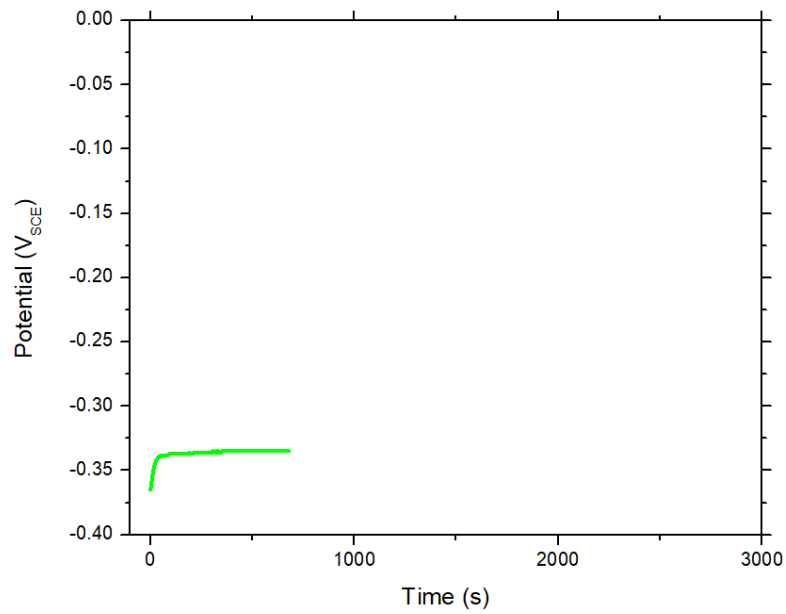


Figure A8: OCP curve AlTiN sample 2.

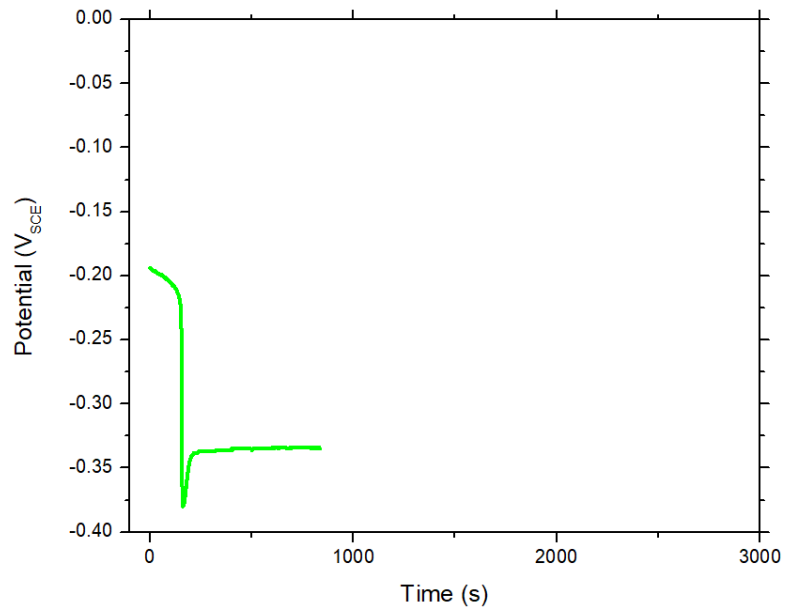


Figure A9: OCP curve AlTiN sample 3.

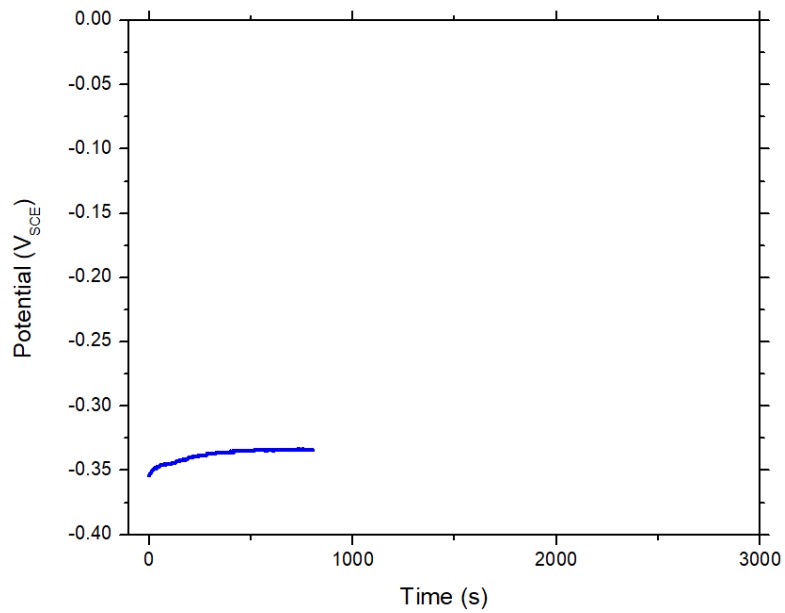


Figure A10: OCP curve SDSS sample 1.

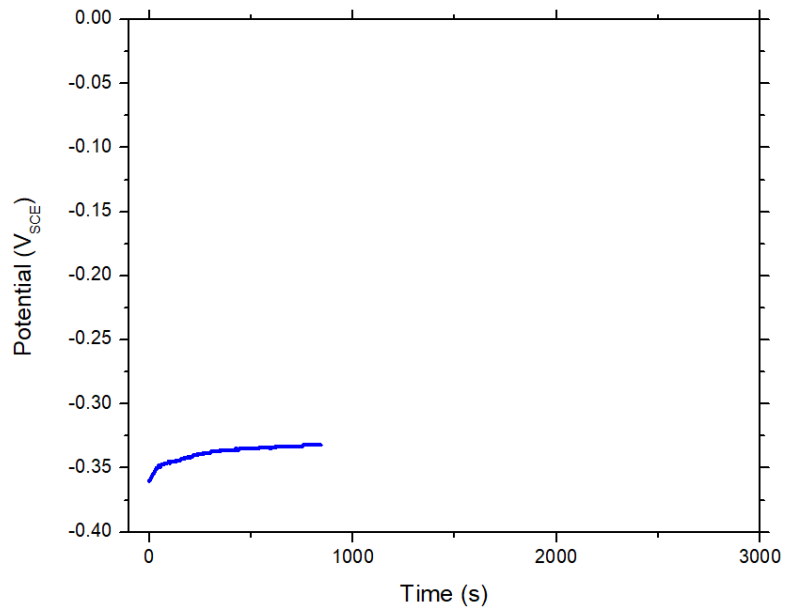


Figure A11: OCP curve SDSS sample 2.

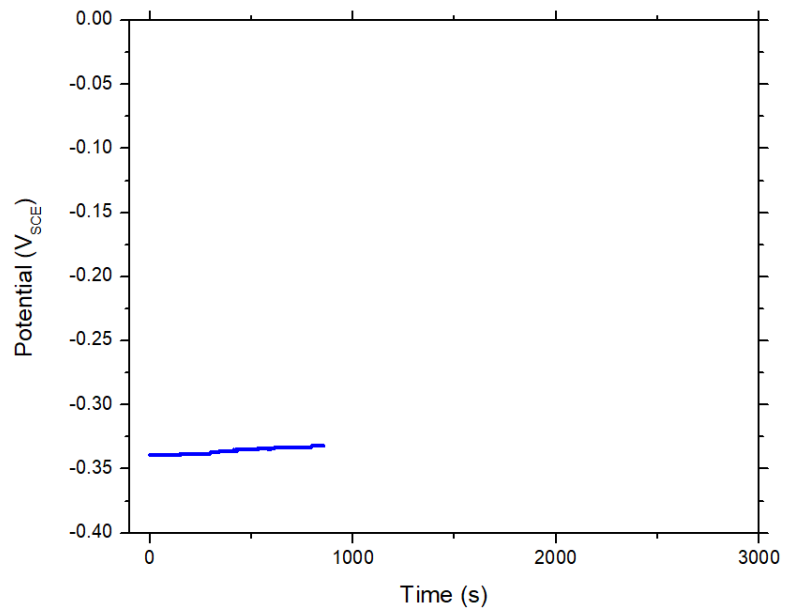


Figure A12: OCP curve SDSS sample 3.

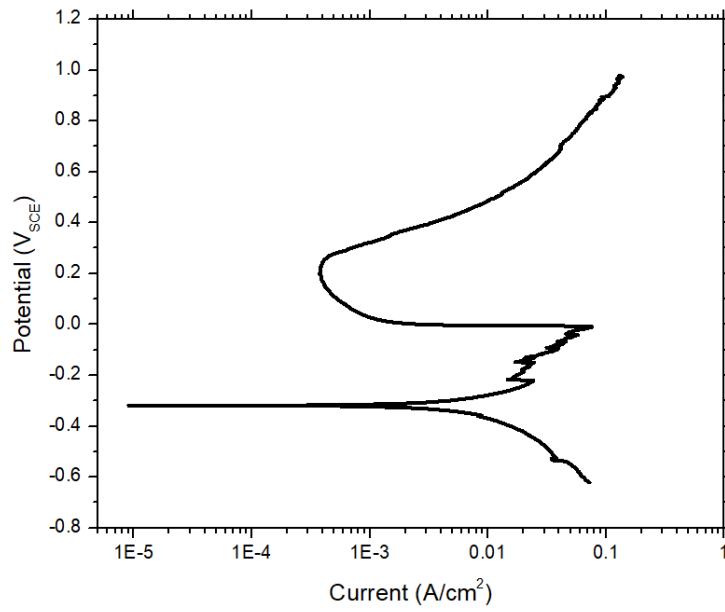


Figure A13: Polarization curve AlCrN sample 1.

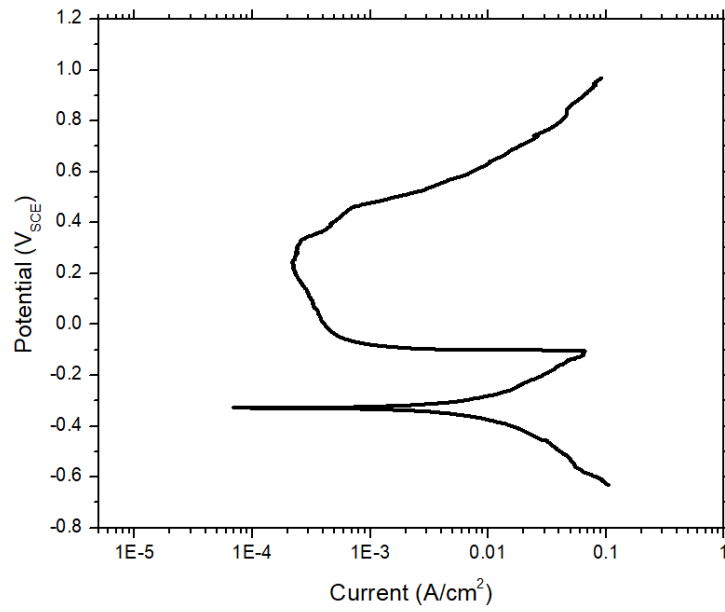


Figure A14: Polarization curve AlCrN sample 2.

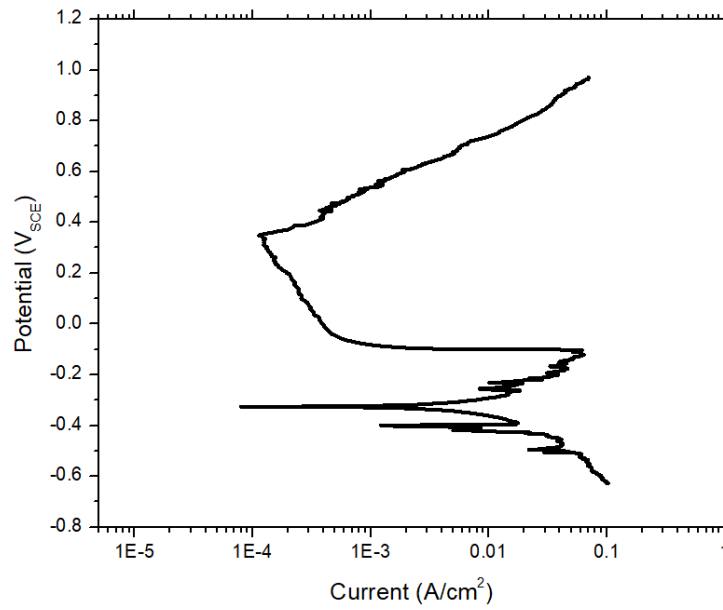


Figure A15: Polarization curve AlCrN sample 3.

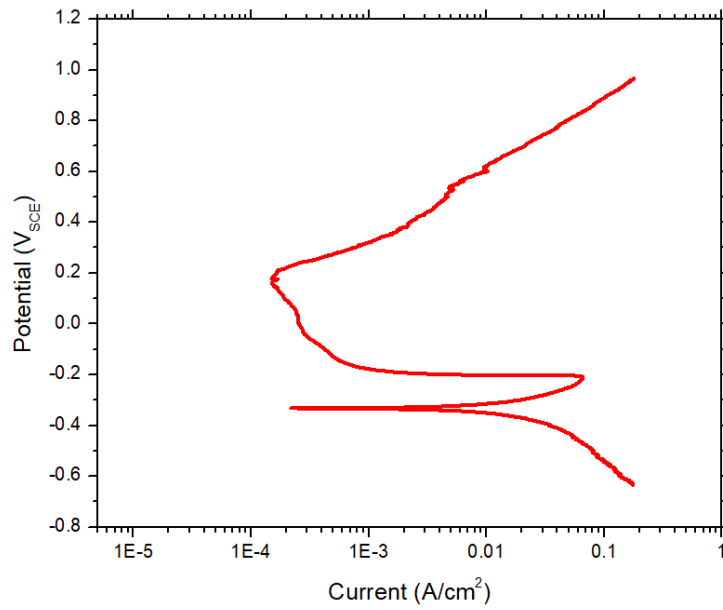


Figure A16: Polarization curve AlCrN/TiSiN sample 1.

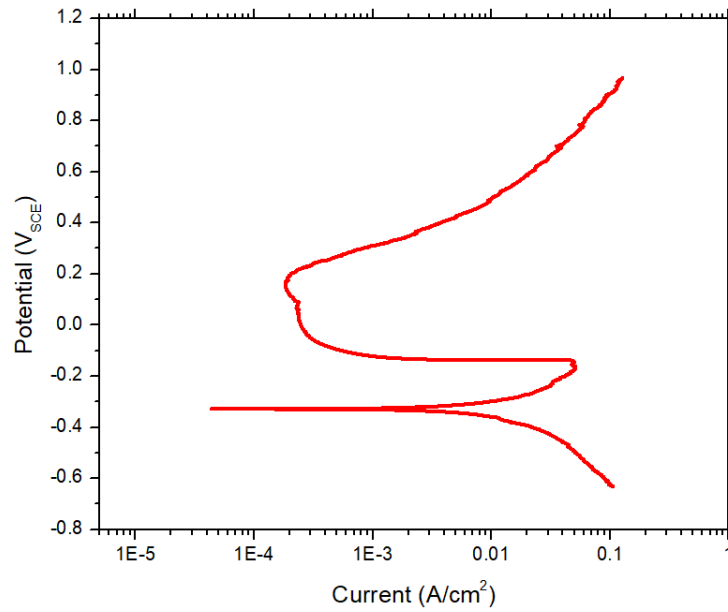


Figure A17: Polarization curve AlCrN/TiSiN sample 2.

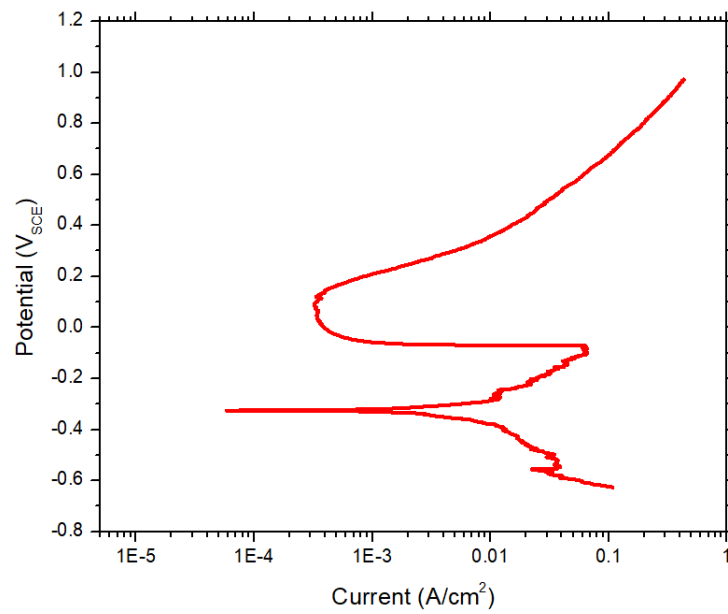


Figure A18: Polarization curve AlCrN/TiSiN sample 3.

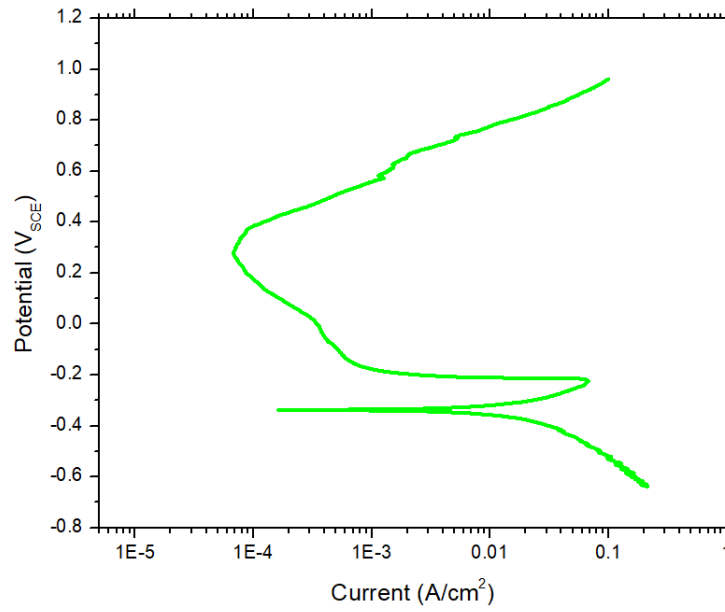


Figure A19: Polarization curve AlTiN sample 1.

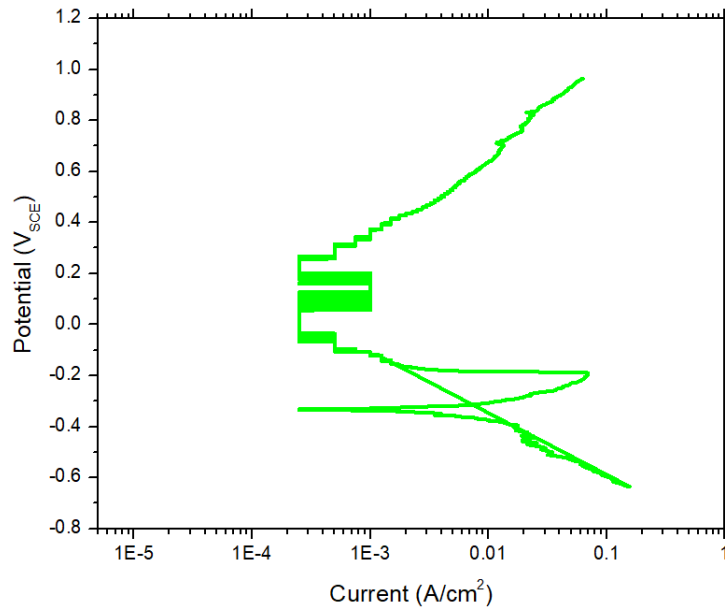


Figure A20: Polarization curve AlTiN sample 2.

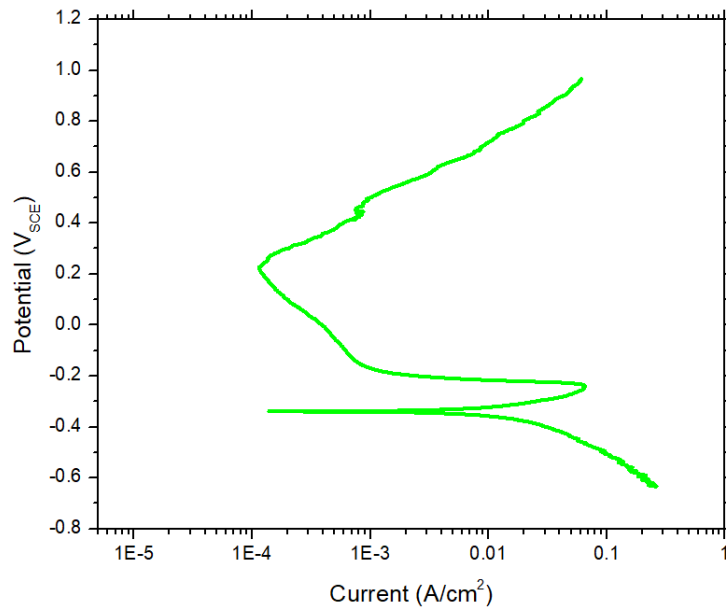


Figure A21: Polarization curve AlTiN sample 3.

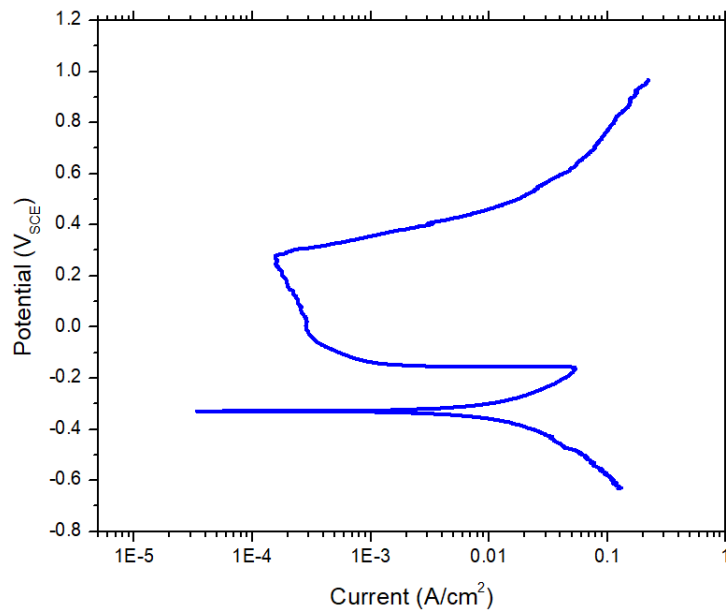


Figure A22: Polarization curve SDSS sample 1.

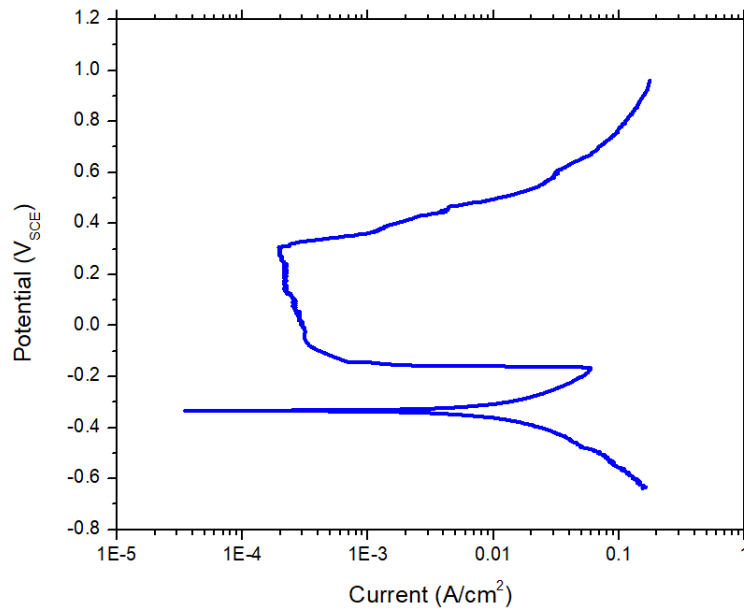


Figure A23: Polarization curve SDSS sample 2.

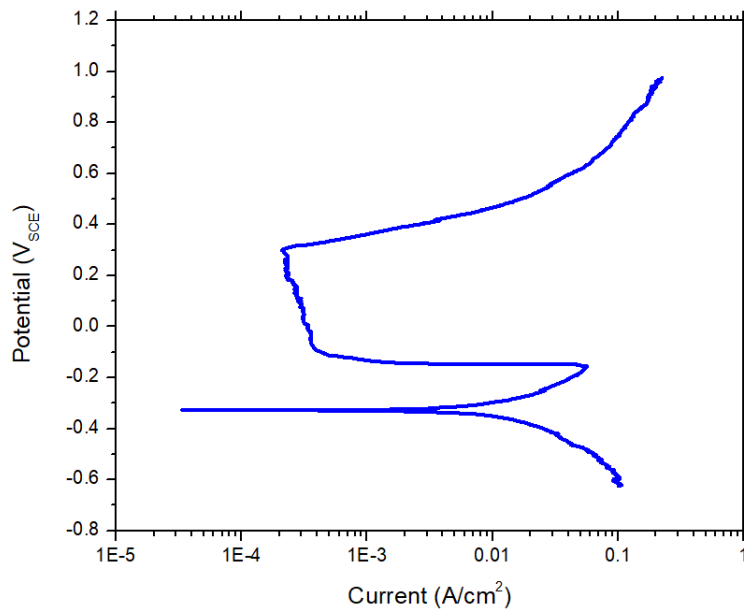


Figure A24: Polarization curve SDSS sample 3.